Conformational Changes of Wild-type SOD1 Affect the Dimerization at Ambient Temperature

by

Günseli Yıldırım

A Dissertation Submitted to the
Graduate School of Sciences and Engineering
in Partial Fulfillment of the Requirements for
the Degree of

Master of Science

in

Molecular Biology and Genetics

KOÇ
ÜNİVERSİTESİ

July 20, 2022

Conformational Changes of Wild-type SOD1 Affect the Dimerization at Ambient Temperature

Koç University

Graduate School of Sciences and Engineering

This is to certify that I have examined this copy of a master's thesis by

Günseli Yıldırım

and have found that it is complete and satisfactory in all respects,
and that any and all revisions required by the final
examining committee have been made.

Committee Members:

Assist. Prof. Hasan Demirci (Advisor)

Prof. Ayşe Nazlı Başak (Co-Advisor)

Prof. Soichi Wakatsuki

Assoc. Prof. Nurhan Özlü

Assist. Prof. Serkan Kır

Date: 20.07.2022

Dedicated to the memory of my grandmother,

Ayşe Leyla Ocak.

ABSTRACT

Conformational Changes of Wild-type SOD1 Affect the Dimerization at Ambient Temperature

Günseli Yıldırım

Master of Science in Molecular Biology and Genetics

July 20, 2022

Amyotrophic lateral sclerosis is a neurodegenerative disease caused by the degeneration of lower and upper motor neurons in the brain and spinal cord. Although ALS is rare, it is the third most common neurodegenerative disease comes after Alzheimer's and Parkinson's. Since ALS has a complex molecular background, there is no effective treatment for this disease. 90% of ALS patients are sporadic, and 10% have familial disease. Mutations in more than 25 genes account for 70% of familial ALS and also explain <10% of sporadic ALS.

SOD1, the second most common ALS-causative gene, encodes the dimeric antioxidant superoxide dismutase 1 protein. More than 180 mutations in the SOD1 gene are associated today with ALS. However, their mechanisms leading to ALS are not fully known. Although most of the mutations appear to have similar pathological effects on protein structure and motor neurons, they lead to different consequences in terms of disease progression. Mutations in SOD1 cause misfolding of immature intermediate form of SOD1 and disrupt the stable dimer structure of the protein; oligomerization and accumulation of the protein occurs in the cytosolic region and at the outer mitochondrial membrane of motor neurons. It has been suggested that misfolded SOD1 may interact with a voltage-dependent anion channel (VDAC1) located at the outer membrane of the mitochondria and prevents entrance of NADH, anions and ATP required for oxidative phosphorylation. On the other hand, macrophage migration inhibitory factor (MIF) is suggested to act as a chaperone for the SOD1 protein, helping misfolded SOD1 fold correctly. This thesis includes i) overexpression and purification of wild-type SOD1, $SOD1^{G93A}$, MIF and VDAC1, ii) crystallization of both wild-type and mutant forms of SOD1 and iii) diffraction data collection from wild-type SOD1. In this study, we attempted to determine the first ambient temperature X-ray structure of SOD1 and identified a wild-type apo SOD1 protein structure at 4.00 Å resolution and P 21 21 21 space group.

ÖZETÇE

Yabanıl Tip SOD1'deki Oda Sıcaklığında Dimerleşmeyi Etkileyen Yapısal Değişiklikler

Günseli Yıldırım

Moleküler Biyoloji ve Genetik, Yüksek Lisans

20 Temmuz 2022

Amiyotrofik Lateral Skleroz (ALS), beyin ve omurilikte bulunan alt ve üst motor nöronların dejenerasyonu sonucu oluşan bir nörodejeneratif bir hastalıktır. Her ne kadar nadir hastalıklar kategorisinde olsa da, bu hastalık Alzheimer ve Parkinson hastalıklarından sonra en çok görülen nörodejeneratif hastalıktır. ALS, karmaşık bir altyapıya sahip bir hastalık olduğu için, etkin bir tedavisi bulunmamaktadır. ALS tanısı konulan hastaların %90'ı sporadik olarak tanımlanırken geri kalan %10'u ise aile geçmişine sahiptir. 25'ten fazla gende bulunan mutasyonların %70 oranında ailesel ALS'yle ilişkili olduğu gösterilmiştir. Sporadik vakalar için bu oran yaklaşık %10'dur.

Süperoksit dismutaz 1 proteinini kodlayan SOD1 geni ailesel ALS'ye en çok neden olan ikinci gendir. Bu gende meydana gelen 180'den fazla mutasyonun ALS ile ilişkili olduğu gösterilmiştir. Fakat, bu proteinin hastalık yapıcı mekanizması hala tam olarak anlaşılamamıştır. Proteindeki mutasyonların protein ve motor nöronlarda benzer patolojik özelliklere sahip olduğu görülse de hastalığın seyri açısından farklı özelliklere sahiptir. Genel olarak, bu gende meydana gelen mutasyonlar proteinin ara tam katlanmamış ara formuna etki ederek proteinin yanlış katlanmasına ve hücre içinde ve mitokondri membranında birikimine neden olur. Yanlış katlanan bu proteinin mitokondri membranında bulunan voltaj-bağımlı anyon kanalı ile etkileşime girerek bu kanal proteininden oksidatif fosforilasyon için gerekli olan NADH, ADP ve anyonların geçişini engellediği gösterilmiştir. Diğer yandan, normalde sitokin olarak görev yapan makrofaj göçü engelleyici faktör (MIF) bu yanlış katlanan proteine bağlanarak düzgün katlanmasına yardımcı olmaktadır. Bu tez kapsamında yapılan çalışmalar, $SOD1^{WT}$, SOD1G93A, MIF proteinlerinin üretimi ve saflaştırması, SOD1'in hem yabanıl hem de mutant formlarının kristalizasyonu ve elde edilen kristallerden X-ray kristalografi yöntemi ile kırınım datalarının elde edilmesidir. Yapılan bu çalışmada apo SOD1'in fizyolojik sıcaklıkta yapısının belirlenmesi hedeflenmiştir ve ön data olarak ilk üç boyutlu X-ray yapısı 4.00 Å çözünürlükle ve P 21 21 21 uzay grubu simetrisinde çözülmüştür.

ACKNOWLEDGEMENTS

Firstly, I would like to express my deepest appreciations to my thesis advisor Assistant Professor Hasan Demirci for his supports and valuable suggestions in this project. It was my greatest pleasure to be one of his first students and be a part of his team, KUYBIIG-M. He inspired me to be a successful scientist and has always motivated me to become stronger every day. He encouraged me not to give up even when the road got tough. I also would like to express my heartfelt gratitude to my co-advisor, Professor Ayşe Nazlı Başak for giving me an opportunity to work with her. It was a great honour for me to work with an expert like her within this project's scope.

I also would like to thank my other thesis committee members, Professor Soichi Wakatsuki, Associate Professor Nurhan Özlü and Assistant Professor Serkan Kır, for their time evaluating my thesis studies. I wish to extend my special thanks to the Graduate School of Science and Engineering personnel for their assistance during writing my thesis. I am also thankful to TUBITAK 2232 International Fellowship for Outstanding Researchers Program (Project No: 118C270) for their financial supports of the project and my master's education.

I am also grateful to all KUYBIIG-M members for their supports and cooperations. Special thanks to Sabri Özkan Besler for never leaving me alone on this journey. It was very valuable to work with him in great synergy during this project. He is more than a great colleague, a friend that I can reach out to whenever I need him. He has been my biggest psychological supporter in all ups and downs. I deeply thank to newcomers of KUYBIIG-M İlkin Yapıcı, Nilüfer Baldır, Cahine Kulakman and Bilge Tosun for their great psychological supports and precious friendships in such a short time. I would love to spend more time with them and have the opportunity to work more. I also would like to extend my special thanks to Esra Ayan, Ebru Destan, Gözde Karakadıoğlu, Nurettin Tokay, Fatma Betül Ertem and Mehmet Gül for their invaluable friendships.

Words cannot express my gratitude to my dear mother Nebat Eser Yıldırım, who is my biggest supporter in my life and the person who helped me achieve these successes. I also sincerely thank my father and brothers for believing in me forever. I would like to

express my most special and final thanks to my boyfriend, Burak Meriç, for being with me since the first day of my studies and supporting me in every moment of my life.

TABLE OF CONTENTS

LIST OF TABLES

LIST OF FIGURES

ABBREVIATIONS

Å	Angstrom
α	Alpha
β	Beta
γ	Gamma
µg	Microgram
µL	Microliter
ADP	Adenosine Diphosphate
ALS	Amyotrophic Lateral Sclerosis
ALS2	Alsin
ATP	Adenosine Triphosphate
Bcl-2	B-cell Lymphoma 2
C	Celsius
Ca	Calcium
CHMP2B	Charged Multivesicular Body Protein 2B
CNS	Central Nervous System
Cu	Copper
DCTN	Dynactin
DNA	Deoxyribonucleic Acid
ER	Endoplasmic Reticulum
ERAD	Endoplasmic Reticulum-associated Protein Degradation
RNA	Ribonucleic Acid
E. coli	*Escherichia coli*
FIG4	Polyphosphoinositide 5-phosphatase
FPLC	Fast Protein Liquid Chromatography
FUS	Fused in Sarcoma
G	Gram
H_2O_2	Hydrogen Peroxide
hCCS	Human Copper Chaperone for Superoxide Dismutase
HCl	Hydrochloric Acid
His-tag	Histidine tag
IPTG	Isopropyl-β-D-thiogalactoside

K	Kelvin
K	Potassium
KARS	lysyl-tRNA Synthetase
kDa	Kilodalton
L	Liter
LB	Lysogeny Broth
mg	Milligram
MIF	Macrophage Migration Inhibitory Factor
min	Minute
miRNA	MicroRNA
mL	Milliliter
M	Molar
mM	Millimolar
mRNA	Messenger RNA
mtDNA	Mitochondrial DNA
Na	Sodium
NaCl	Sodium Chloride
NADH	Nicotinamide Adenine Dinucleotide + Hydrogen
Ni-NTA	Nickel-Nitrilotriacetic Acid
O_2	Oxygen
O_2^-	Superoxide
OD	Optical Density
PDB	Protein Data Bank
PFN1	Profilin 1
RMSD	Root Mean Square Deviation
ROS	Reactive Oxygen Species
rpm	Revolutions per minute
SDS-PAGE	Sodium Dodecyl Sulfate Polyacrylamide Gel Electrophoresis
SOD1	Superoxide Dismutase 1
SQSTM1	Sequestosome 1/p62
OPTN	Optineurin
TBK1	Tank-binding Kinase 1
TDP-43	TAR DNA Binding Partner-43

Tris	Tris(hydroxymethyl)aminomethane
UBQLN2	Ubiquilin
VAPs	VAMP-associated Proteins
VCP	Valosin-containing Protein
WT	Wild-type
Zn	Zinc

Chapter 1:
INTRODUCTION

1.1 Amyotrophic Lateral Sclerosis

Amyotrophic Lateral Sclerosis (ALS), also known as 'Lou Gehrig's disease,' is a progressive, fatal adult-onset neurodegenerative disease that affects upper and lower motor neurons in the brain and spinal cord and causes muscle wasting in several parts of the body. Although it is classified as a rare disease, ALS is one of the most common neurodegenerative diseases (Chio et al., 2013; Brown & Al-Chalabi, 2017; Talbot et al., 2018; Vahsen et al., 2021). Motor neurons (MNs)which have unique shapes characterized by their long axons. MNs can be grouped into two main types of neurons, depending on their location; i) upper motor neurons located in the motor cortex and ii) lower motor neurons in the ventral horn of the spinal cord and brainstem (Stifani, 2014). Clinical symptoms of the disease are distinguished according to the origin of the primary pathology; generally, lower motor neuron degeneration results in weakness, muscle atrophy, and fasciculations, and upper motor neurons cause spasticity and awkward movements (Mulder et al., 1986).

Symptoms may present with weakness in the arms and legs or difficulty with tongue movements, chewing, and swallowing. As the disease progresses severe symptoms such as weakening of all skeletal muscles and fatal respiratory problems can be seen. As a result of these painful symptoms, patients die within 2-5 years from the diagnosis (Chio et al., 2013). Although this disease generally occurs in adulthood, symptoms may begin to appear in the patient's early years. The mean age at onset of the disease is 55 years (Taylor et al., 2016).

Incidence of the disease differs depending on the origin place in the world; European countries have the highest number with an incidence of >3 in 100.000 people per year. This value is much lower in east and south Asia (~0.8 and ~0.7 in 100.000) (Talbott et al., 2016).

1.2 Pathological Mechanisms of ALS

Although the underlying mechanism of motor neuron degeneration which causes ALS is still unclear nowadays, some hallmark cellular pathological changes may cause it. These include mutations of several genes, disruption of protein homeostasis, impaired RNA processing, disrupted axonal transport, neuroinflammation, mitochondrial dysfunction and oxidative stress (**Figure 1.1**).

1.2.1. Genetic Background of ALS

The majority of ALS cases, 90% are sporadic, and the remaining 10% are hereditary, classified as familial ALS. More than 25 genes are primarily associated with familial ALS, but sporadic cases might also have unclear hereditary with a complex genetic background (Renton et al., 2014). Most of these genes are inherited autosomal dominant and have high penetration and also hereditability of sporadic cases without familial origin is approximately 60% of sporadic cases (Al Chalabi et al., 2010). Even though genetic variations that cause the disease seem to affect a minority of the patients, they are crucial to understanding pathological mechanisms of ALS through the proteins encoded by these genes.

Mutations in the C9orf72 gene cause the GGGGCC (G4C2) repeat expansions in the intronic region of this gene, this is the most common genetic cause of the disease (40%) (Renton et al., 2011; Majounie et al., 2012). The average number of G4C2 repeats in the C9orf72 gene seen in a healthy person is 30. However, in C9orf72 mutations related ALS, this number might be hundreds or even thousands (DeJesus-Hernandez et al., 2011). Several pathological mechanisms are caused by the abnormal expansion of hexanucleotide repeats in this gene. As a result of the mutation, RNA foci have an unexpected secondary structure, bind to nuclear proteins, and cause insoluble fractions in the nucleus (Donelly et al., 2013; Lagier-Tourenne et al., 2013). On the other hand, RNA products caused by of repeat expansion may escape from the nucleus to cytosol and generate toxic dipeptide repeats by a noncanonical translation process (Peters et al., 2015). The second most common causative and first identified gene of ALS disease is superoxide dismutase 1(SOD1). ~20% of fALS and 1-3% of sALS cases result from missense SOD1 mutations (Rosen et al., 1993; Zou et al., 2017). ALS-related mutant SOD1 results in misfolding and oligomerization of the protein. Misfolded proteins

aggregate in the cytosol and the membrane of mitochondria of motor neurons (Pasinelli et al., 2004; Pickles et al., 2013; Benkler et al., 2018). There are also ALS-related genes that encode proteins responsible for RNA processing; TAR DNA binding partner 43 (TDP-43) (5% of cases) and Fused in Sarcoma (FUS) (5% of cases). Mislocalization of these proteins causes accumulation of aggregates in the cytosolic part and disruption of several mechanisms, including mRNA splicing and miRNA biogenesis (Kwiatkowski et al., 2009; Vance et al., 2009; Prasad et al., 2019). Although these four genes are involved in most of the cases, other genes that have roles in different mechanisms have been identified; SQSTM1, OPTN, TBK1, VAPs, UBQLN2, VCP, CHMP2B, ALS2, FIG4, PFN1, DCTN (Yang et al., 2001; Cox et al., 2010; Johnson et al., 2010; Maruyama et al., 2010; Deng et al., 2011; Fecto et al., 2011; Sanhueza et al., 2013; Liu et al., 2014; Smith et al., 2015) (**Table 1.1**).

Table 1.1 Genes are related to ALS

Gene Name	Protein	Function	Inheritance
C9orf72	Chromosome 9 opening reading frame 72	Cellular trafficking via actin, and regulation of lysosome biogenesis and maturation.	Autosomal dominant
SOD1	Superoxide dismutase 1	Antioxidant enzyme: uses copper to convert superoxide radical species to oxygen or hydrogen peroxide.	Autosomal dominant, recessive
FUS	Fused in sarcoma	Regulation of several RNA related mechanisms; mRNA splicing, processing, transport, and translation.	Autosomal dominant
TDP-43	TAR DNA binding partner 43	Regulation of several RNA related mechanisms; mRNA splicing, processing, transport, and translation.	Autosomal dominant
SQSTM1	Sequestosome 1/p62	recruit cargo to autophagy.	Autosomal dominant
OPTN	Optineurin	Recruit cargo for autophagy process	Autosomal dominant
TBK1	Tank-binding kinase 1	Phosphorylation of p62, OPTN for autophagy.	Autosomal dominant

VAPB and VAPC	VAMP-associated proteins B and C	Activation of endoplasmic reticulum-associated protein degradation (ERAD) and autophagy.	Autosomal dominant
UBQLN2	Ubiquilin	Recognition ubiquitinated proteins.	X-linked disease
VCP	Valosin-containing protein	Forming aggresomes and translocation them out of ER for degradation.	Autosomal dominant
CHMP2B	Charged multivesicular body protein 2B	Generating multi-vesicular bodies (MVBs).	Autosomal dominant
ALS2	Alsin	Generating MVBs	Autosomal recessive
FIG4	Polyphosphoinositide 5-phosphatase	Generating MVBs.	Autosomal dominant
PFN1	Profilin1	Cytoskeleton protein responsible for transport within cells.	Autosomal dominant
DCTN	Dynactin	Cytoskeleton protein responsible for transport within cells.	Autosomal dominant

1.2.2. Disruption of Protein Homeostasis

Protein homeostasis provides a network responsible for balancing the production and degradation of proteins and is fundamental to all cellular mechanisms in the body. The accumulation of aggregated proteins in the cellular part of upper and lower motor neurons is one of the neuropathological findings of ALS. The most common ALS-related proteins like SOD1, C9orf72, TDP-43 and FUS can form aggregates in the cytosolic part of neurons or on components of protein homeostasis such as mitochondria, ER, and proteasome (Watanabe et al.,2001; Wang et al., 2002; Kwiatkowski et al., 2009; Cooper-Knock et al., 2012). Impaired protein homeostasis in motor neurons is mainly related to the disruption of ubiquitin-dependent protein degradation and autophagy mechanisms. In ubiquitin-dependent protein degradation, proteins are ubiquitinated by ubiquitin enzymatic cascade and then degraded by proteasome complex. Autophagy is another mechanism involving the degradation and recycling of proteins and cytoplasmic organelles. Some mutations of proteins (C9ORF72, OPTN, SQSTM1, VCP, and

UBQLN2) are also involved in the autophagy mechanism or ubiquitin-proteasome system (Majcher et al., 2015; Ying and Yue, 2016; Nassif et al., 2017).

1.2.3. Impaired RNA Processing

Two essential ALS-related genes encode RNA-binding proteins, TDP-43 and FUS, which are involved in the RNA processing mechanisms, including mRNA splicing, transport, and translation. TDP-43 and FUS are proteins located in the nucleus under normal conditions. Mutation in the TDP-43 and FUS genes causes mislocalization and aggregation of these proteins in the cytosolic part of the cell. The cause of RNA-binding proteins-related ALS is unknown since they have different roles in cells (Neumann et al., 2006; Kwiatkowski et al., 2009; Vance et al., 2009).

1.2.4. Disrupted Axonal Transport

Axonal transport is the mechanism responsible for transferring cellular cargo components like proteins, organelles, vesicles, and lipids to the end of the axon. It is essential for maintaining the cytoskeleton and the communication between presynaptic and postsynaptic neurons. Abnormalities in axonal transport are commonly seen as pathological changes in neurodegenerative diseases (Perlson et al., 2010; Millecamps and Julien, 2013). Alterations in neurofilament an essential component of axonal transport, such as overexpression, over phosphorylation of neurofilament subunits, or mutations in the genes that encode neurofilament subunits may cause accumulation of neurofilaments. This disorganization of neurofilaments can cause ALS pathogenesis in motor neurons. Within mutations in DCTN1, defects of the dynein-dynactin complex in the microtubules reduce retrograde transport by accumulating neurofilaments and causing degeneration in neurons (Kieran et al., 2005). Besides axonal transport components, mutations in the ALS-related genes might be responsible for deficits in axonal transport. Previous studies have shown that SOD1 mutations are also associated with slow antegrade and retrograde transport, they affect the transport even before degeneration in neurons (Murakami et al., 2001; Moller et al., 2017). The other ALS-related protein, TDP-43, typically binds to neurofilament light chain mRNA and has a role in the processing of this mRNA and regulation of splicing another axonal component, peripherin (Strong et al., 2007).

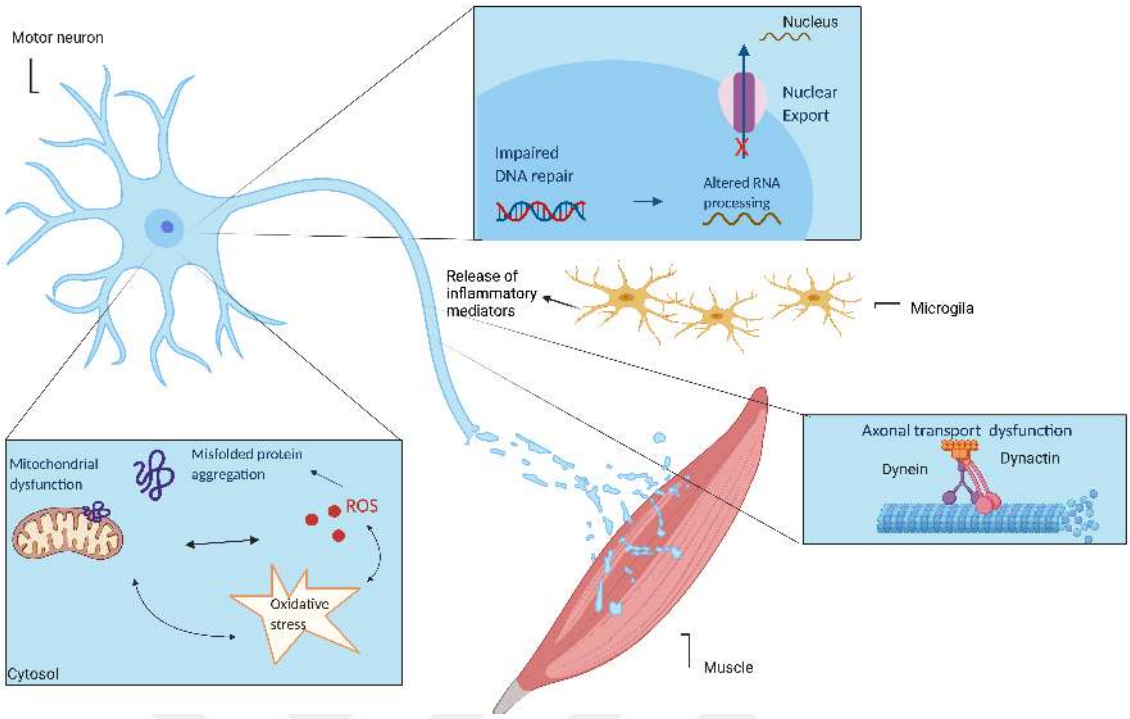

Figure 1.1 The main mechanisms involved in the pathogenesis of ALS in degenerated motor neurons
In the top left panel, oxidative stress-related cellular defects are shown. The top right panel shows the effect of impaired DNA repair on RNA processing in the nucleus. The bottom right panel represents the disruption of microtubules and axonal transport dysfunction.

1.2.5. Neuroinflammation by Microglia and Astrocytes

Neuroinflammation, activated by astrocytes and microglia, is one of the pathogenic hallmarks associated even with the pre-symptomatic phase of ALS. Previous in vivo studies have shown that the accumulation of misfolded proteins like SOD1 might be responsible for the activation of microglia in the early stages of ALS (Boillée et al., 2006). When microglia are activated and overproduce inflammatory elements like cytokines and chemokines, it provokes the neurotoxic effect of astrocytes in oligodendrocytes and neurons (Harry et al., 2008). Recent studies suggest that the response resulting from microglia activation causes the degeneration of motor neurons (Hickman et al., 2018). Inflammatory cytokines and chemokines were found in abundance in ALS patients' cerebrospinal fluid and blood samples (Kuhle et al., 2009)

and ALS-related mutant proteins which are expressed in astrocytes also lead to death of motor neurons (Tong et al., 2013; Kia et al., 2018).

1.2.6. Mitochondrial Dysfunction and Oxidative Stress

The mitochondrion is the prominent organelle that produces the required ATP for cellular activities. Besides this well-known function of mitochondria, they are also essential components for calcium homeostasis and regulation of apoptosis. Mitochondrial abnormalities in neurons are highly related to the pathogenesis of several neurodegenerative diseases, including ALS (Wang et al., 2019). The first identified mitochondrial abnormality in ALS is the morphologically altered and accumulated mitochondria in neurons of ALS patients (Atsumi, 1981). Alterations in the structure of mitochondria were also reported in mouse and cell models of ALS. In addition, *in vivo* studies have shown that overexpression of certain mutant ALS-related proteins results in morphological changes in mitochondria (Kodavati et al., 2020). One of the essential functions of mitochondria in neurons is having a calcium buffering system. Disruption of ER-mitochondria communication in the cells may cause the impaired calcium buffering (Ryan et al., 2020). Decreased reuptake of calcium by mitochondria results in excessive amounts of cytosolic calcium and motor neuron death (Kawamata and Manfredi, 2010).

Although morphological changes in mitochondria are associated with the pathogenesis of ALS disease, mitochondrial dysfunction also affects motor neurons in many ways. The accumulation of ALS-related misfolded proteins such as SOD1, TDP-43, FUS and C9orf72 in the mitochondrial membrane is the most important factor causing mitochondrial dysfunction in both fALS and sALS (Magrane et al., 2009; Wang et al., 2013; Blokhuis et al., 2013). Generally, they do not just accumulate in mitochondria but also interact with mitochondrial proteins. It has been shown that the location of mutant SOD1 on the mitochondrial membrane and interaction between mutant SOD1 and some mitochondrial proteins leads to reduced activation of the electron transport chain by preventing the entrance of ions, metabolites and ADP required for oxidative phosphorylation and ATP production (Mattiazzi et al., 2002). Accumulation of mTDP-43 in mitochondria affects energy transformation by binding to mRNA of mtDNA-encoded complex I subunits (Wang et al., 2016). Interaction between FUS and

mitochondrial chaperone HSP60 also causes decreased ATP production and increased production of reactive oxygen species (ROS) by mitochondria (Deng et al., 2015).

1.3 Overview of Superoxide Dismutase 1 (SOD1)

Superoxide dismutase 1, an antioxidant protein, is expressed almost in all human cells**.** This protein has a role in converting superoxide (O_2^-) free radicals, very toxic to the cellular environment, to O_2 and H_2O_2 by reducing Cu^{2+} to Cu^+ and then oxidizing back (McCord and Fridovich, 1966) (**Figure 1.2**).

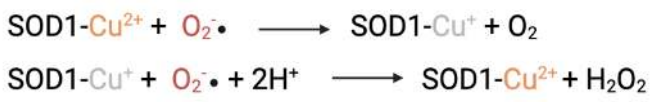

Figure 1.2 The reaction of converting superoxide to oxygen and hydrogen peroxide by SOD1

SOD1 is a 16 kDa protein and its fully mature form is a 32 kDa homodimeric enzyme and each monomer of the protein contains eight stranded β-barrel motif, intra-subunit disulfide bonds and copper (Cu^{2+}) and zinc (Zn^{2+}) binding sides (Huai and Zhang, 2019). Although it binds to copper ions to catalyze the reaction of converting superoxide to less harmful molecules, zinc-binding provides a more stable structure for the protein (Yang et al., 2018). Metal-binding and intra and inter-subunit disulfide bonds are the main properties providing the remarkably stable structure of the mature protein and affect each other. Through the formation of disulfide bonds, the protein is stable and functional even in a reducing environment (Sea et al., 2015). Disruption of the intrasubunit disulfide bond formation can cause the loss of metal binding property. On the other hand, Cu/Zu orientation is also crucial for the formation of intra-subunit disulfide bonds (Kayatekin et al., 2010). At the protein's active site, there are six histidine residues (His46, His48, His63, His71, His80, His120) provide copper-zinc binding, two positively charged residues

Lys136 and Arg143 and intra-subunit disulfide bond between Cys57 and Cys146 (**Figure 1.3**).

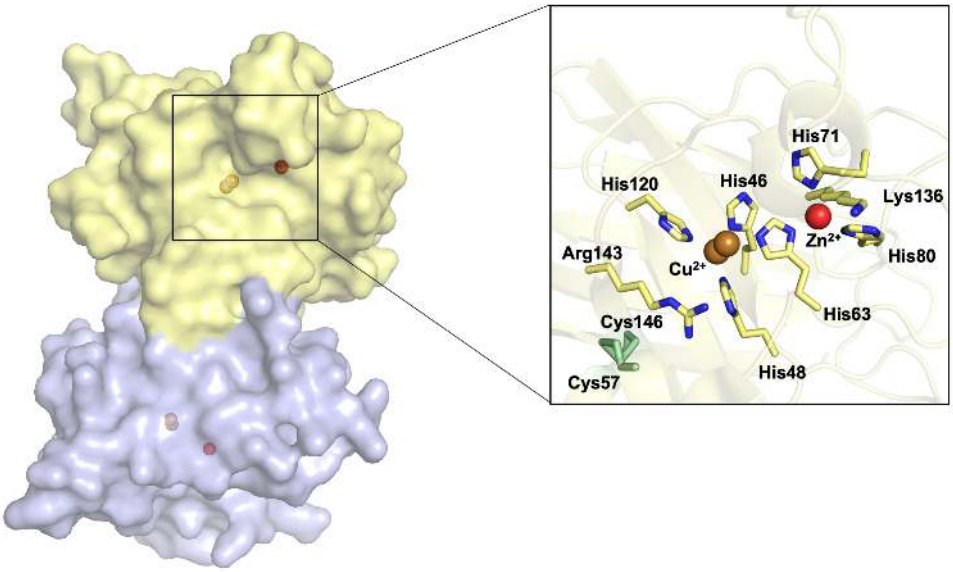

Figure 1.3 Active site of SOD1
Chains are colored pale yellow and light blue. The orange and red spheres represent Cu^{2+} and Zn^{2+} ions, respectively. The disulfide bond between Cys57 and Cys146 is shown in pale green color.

Currently, 217 variants of SOD1 associated with ALS have been reported (https://alsod.ac.uk/output/gene.php/SOD1). In general, most of the mutations are missense and inherited as autosomal dominant (**Figure 1.4**). The phenotype of mutations may change according to the progression and severity of the disease (Pasinelli and Brown, 2006). Although various mechanisms resulting from pathogenic mutations of SOD1 have been suggested, the underlying cause of toxicity is still unclear. It has been shown that mutations related to ALS decrease the activity of the protein by at least 50%. However, the severity of the disease is not correlated with the decrease in enzymatic activity. The cause of ALS related to SOD1 mutation is most probably a toxic gain of function of the misfolded protein by aggregation (Joyce et al., 2011). Conformational changes in the protein may cause misfolding of the immature protein which then goes through oligomerization (Bruijn et al., 1998; Banci et al., 2008). In normal conditions, fully mature SOD1 proteins are localized in the cytosolic part as soluble. Misfolding of the

protein may cause aggregation in the cytosol and on the membranes of mitochondria and endoplasmic reticulum (Vande Velde et al., 2008).

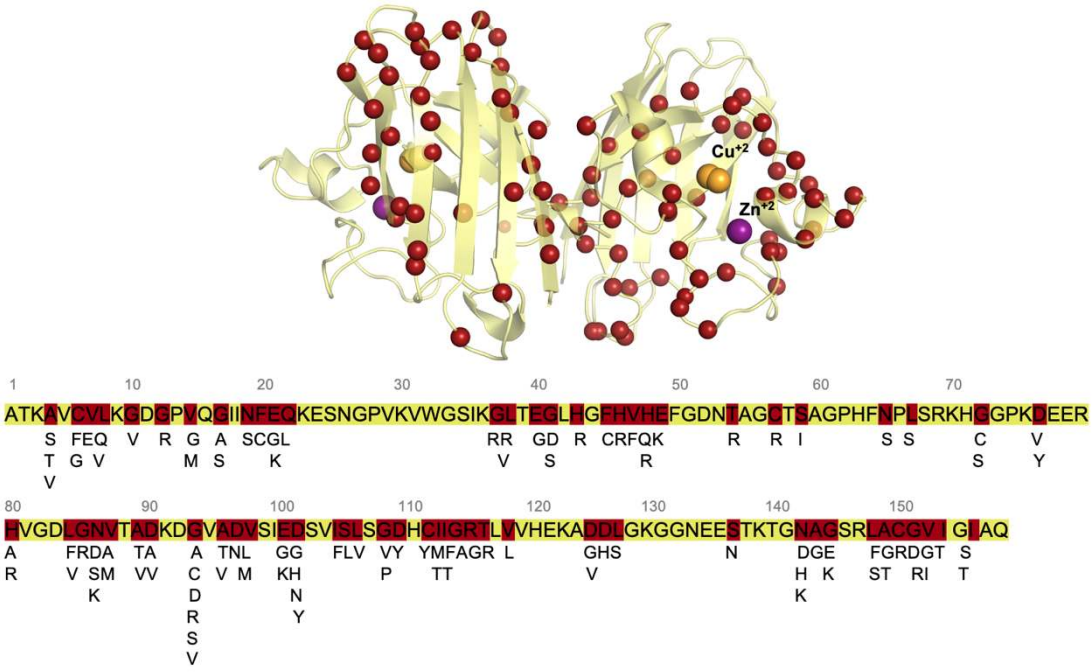

Figure 1.4 The locations of missense mutations of SOD1 in X-ray structure and the amino acid sequence
All firebrick-colored spheres show the point mutations of SOD1.

Mutations in the SOD1 gene may result in non-identical conformational changes in the protein and mediate different misfolded structure variants (Prudencio and Borchelt, 2011). It has been shown that more than 44 different structural states of SOD1 may occur according to their metal binding, disulfide bond formation and oligomerization levels (Furukawa and O'Halloran, 2005). Although all the pathogenic mutations do not have the same structural properties, it has been investigated that they have a similar pattern of creating a toxic environment. These pathogenic mutants might be able to prevent post-translational maturation of the protein. Generally, they destabilize the metal-free immature form with reduced disulfide bonds of the protein and affect metal binding or/and disulfide bond formation. Mutant SOD1s with known effects were categorized into two types: one group affects the metal binding by disturbing electrostatic and zinc-binding loops (H46R, G85R, D124V, D125H, and S134N), while the other one has typical metal-binding properties but sensitive for disulfide bond reducing (A4V, L38V, G41S, D90A, and G93A) (Tiwari et al., 2005; Huai and Zhang, 2019). Although they

have similar structural features, the intracellular effects and toxicity levels of mutations can differ. Therefore, the toxicity caused by mutations is not known.

1.4 Maturation and Oligomerization of SOD1

Although the dimeric structure of SOD1 is stable, during the maturation of the protein, there are several states until it is folded in its native dimer structure. Folding SOD1 to native functional protein is a complex process for a small protein. In the first step of maturation, SOD1 is in a monomer form without metal ions and an intra-subunit disulfide bond (E, E (2SH)). Zn^{2+} binding to the apo form of monomer stabilizes the monomer form of the protein. The protein's zinc-bound state (E, Zn, (2SH)) may also form the dimeric protein. However, this dimeric structure is not as stable as the natively folded protein. This more stable structure recruits human copper chaperone for superoxide dismutase (hCCS) to bind Cu^{2+} ions to each monomer and create Cu, Zn, (2SH) monomers. The following process of metal binding is the oxidation of the protein's metal-bound form. As a result of the oxidation, disulfide bonds between Cys57 and Cys146 are formed. The last step of maturation is when these monomers come together and form a fully mature dimer structure by establishing non-covalent interactions (Banci et al., 2012; Culik et al., 2018). Under normal conditions, all these intermediate forms proceed on the pathway to achieving a fully mature structure. However, in animal models of SOD1-induced ALS and in vivo studies, it has been observed that these metal-free and/or disulfide-free immature structures accumulate in the cell because of misfolding and then form amyloid-like fibrils with growing aggregation (Chia et al., 2010; Ivanova et al., 2014) (**Figure 1.5**).

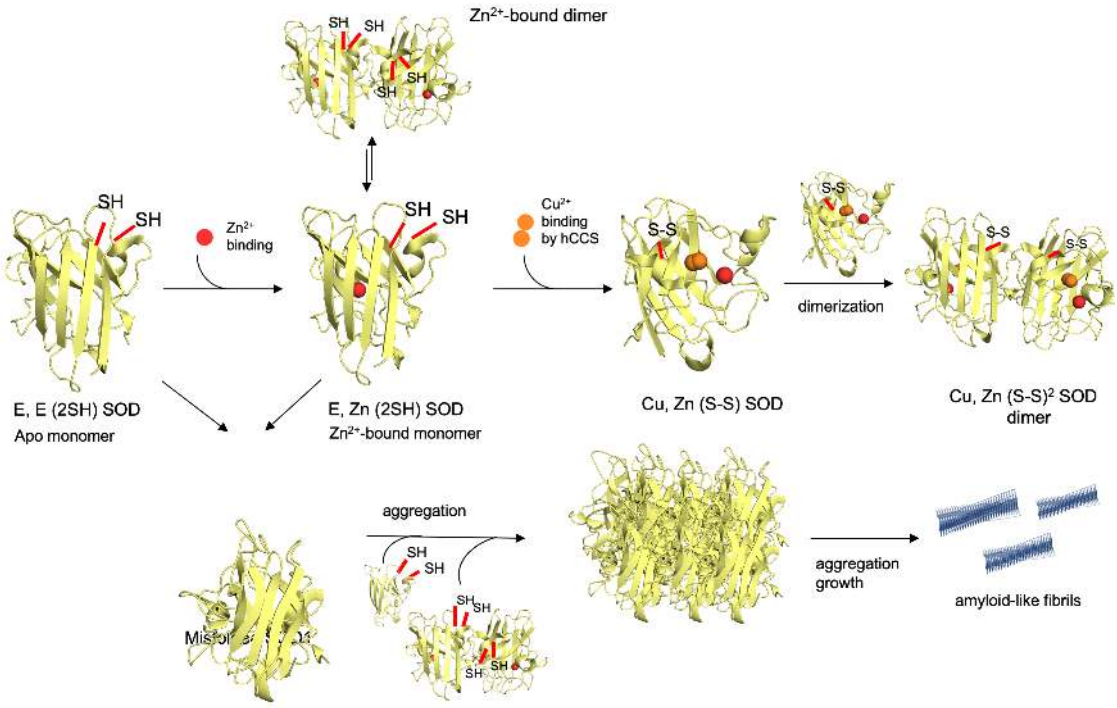

Figure 1.5 The maturation and oligomerization processes of SOD1

1.5 Interaction Partners of SOD1

According to previous studies, it has been suggested that mutations in the SOD1 may cause structural variations of the protein and may result in a toxic gain of function. However, the underlying mechanisms of toxicity are unknown. Interactions between SOD1 and proteins that have roles in different cellular mechanisms have been identified to elucidate the disease mechanisms caused by this protein. One of the causes of oxidative stress and mitochondrial dysfunction, among the most critical mechanisms of ALS, is the accumulation of aggregates formed by mutant SOD1s in the cytosolic part of mitochondria and their interaction with mitochondrial proteins. Misfolded SOD1 directly binds to two vital proteins located on the outer membrane of mitochondria; one is the voltage-dependent anion channel 1 (VDAC1), responsible for the entrance oxidative phosphorylation components such as ions, metabolites, ADP and NADH (Israelson et al., 2010; Shteinfer-Kuzmine et al., 2019), the other one is an anti-apoptotic protein Bcl-2 which has a crucial role in cell survival (Pasinelli et al., 2004). Since binding of SOD1 to these proteins causes conformational changes and affects the activity of these proteins, mutations of SOD1 have been found to be related to mitochondrial dysfunction.

Additionally, the interaction of SOD1 with another mitochondrial protein, lysyl-tRNA synthetase (KARS), an essential protein for mitochondrial protein synthesis, causes

misfolding and aggregation of this protein (Kawamata et al., 2008). It has been shown that the other functionally disrupted organelle by misfolded SOD1 proteins is the endoplasmic reticulum. Misfolded proteins create aggregates and interact with different proteins that have roles in ER. Mainly, they interact with Derlin-1, the part of the ER-associated degradation (ERAD) machine that provides translocation of misfolded proteins from ER to the cytosolic part of the cell. Interaction between these two proteins triggers cellular cytotoxicity and motor neuron death (Nishitoh et al., 2008).

Besides the effects of misfolded SOD1 on mitochondria and ER, it is a transcription factor responsible for regulating oxidative repair and resistance genes. In response to increasing ROS (especially superoxide), it goes from the cytosol into the nucleus. In the nucleus, phosphorylation of SOD1 at S60 and S99 by its effector kinase Dun1/Cds1 promotes the expression of the genes (Banks and Andersen, 2019). Since aggregates have enormous molecular weight accumulated in the cytosol, SOD1 cannot localize into the nucleus and oxidative response is disrupted. Proteins belonging to the proteasome complex are other targets of misfolded SOD1. The proteasome is a complex with two main components: core 20S protease and 19S, with two regulatory subunits showing ATPase activity. Mutant SOD1s bind to two subunits of 19S (S6 and S6') and reduce ATP-dependent activation of proteasome complex and protein degradation (Cheroni et al., 2009). On the other hand, ALS-related mutants of this protein induce the other essential protein degradation mechanism, autophagy, by binding Parkin and SQSTM1 which have a role in the formation of autophagosome complex (Gal et al., 2009; Palomo et al., 2018). Besides its interaction causing toxicity in the cellular environment, it has been reported that binding of MIF to misfolded SOD1 reduces amyloid-like fibril structures and the accumulation of the protein in the cytosol, mitochondrial and ER membranes (Shvil et al., 2018).

1.6 Voltage-dependent Anion Channel 1 (VDAC1)

Mitochondria are organelles with two membranes; the first one is the outer mitochondrial membrane facing the cytosolic part of the cell and the other one is the inner mitochondrial membrane that separates the outer membrane from mitochondrial cytosol. An intermembrane space localizes between these two mitochondrial membranes. The primary function of mitochondria is generating ATP by oxidative phosphorylation. ATP

is produced in the last step of the electron transport chain, which is localized to the inner membrane of the mitochondria.

VDAC1 is a transmembrane protein located in the outer mitochondrial membrane. It is the primary channel for the entrance of the metabolites, ions and nucleotides required for oxidative phosphorylation. VDAC1 is active in the voltage range of -40 to +40 mV, with the best conductivity at 0 mV (Camara et al., 2017). In this range, the channel is in the open position, while the voltages are -40 and above +40 mV, which causes the channel to be closed and reduces its conductivity (Rostovtseva and Colombini, 1996, 1997). It is permeable for the anions, ADP, NADH and metabolites of the respiratory chain in the open state and allows the passage of cations such as Ca2+, Na+ and K+ in the close state (Rostovtseva et al., 2008). It also has an essential role in the apoptotic signaling pathway which is mediated in the mitochondria by interacting with anti-apoptotic protein Bcl-2 and cytosolic kinases of mitochondria, e.g., Hexokinase I (Tsujimoto and Shimizu, 2000; Shimizu et al., 2001).

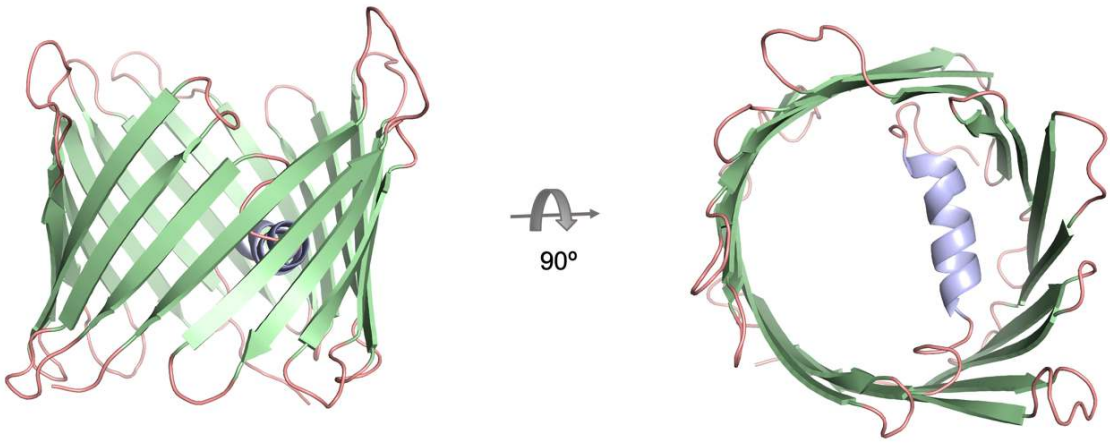

Figure 1.6 The cartoon representation of the side and top view of the VDAC1 structure
β-strands, α-helix and loop regions colored pale green, light blue and dark salmon, respectively.

VDAC1 is a channel containing a hydrophobic 19-stranded β-barrel mounted on the outer membrane and an alpha-helix at the N-terminal located inside the pore (Bayrhuber et al., 2008) (**Figure 1.6**). The conformational changes in the open and close states are still not identified. However, this N-terminal α-helices portion of the protein is thought to move in and out of the pore as it transitions into open and closed states. It has also been suggested that the N-terminal region may be essential in regulating metabolites'

entrance (Geula et al., 2015). In the study of Isrealson et al. (2010), it has been shown that when misfolded mutant SOD1 proteins accumulated on the mitochondrial membrane, they directly bind to VDAC1 and inhibit the entrance of metabolites and ions required for oxidative phosphorylation. Understanding the interaction mechanism between these two proteins will be a major step forward in elucidating mitochondrial dysfunction, one of the most important underlying causes of the disease.

1.7 Macrophage Migration Inhibitory Factor (MIF)

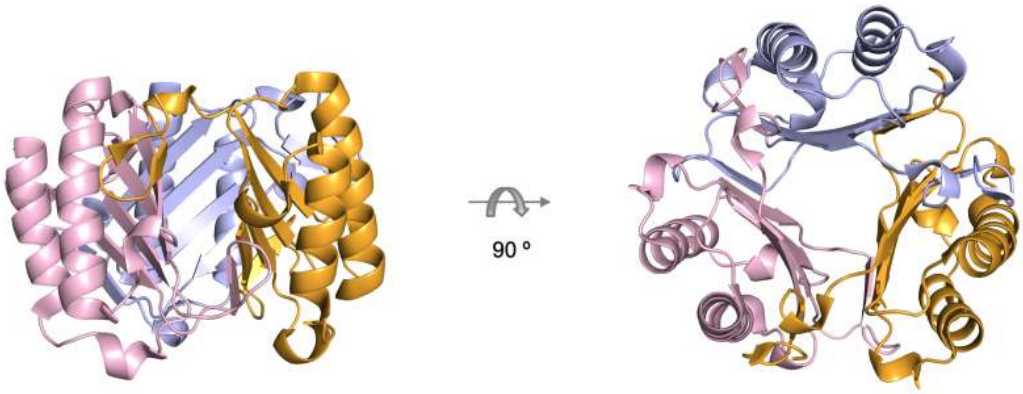

Figure 1.7 Three-dimensional structure of trimeric MIF protein, the side and top view
Monomers are shown in light blue, light pink and orange colors.

Macrophage migration inhibitory factor is a trimer ubiquitous protein with different roles in cells as a cytokine, enzyme and chaperone-like protein (Song et al., 2022). When the protein was discovered, the function of MIF was determined as a cytokine involving immune response in delay hypersensitivity (Bloom et al., 1966). It is also named as such since it prevents the random movement of macrophages. Besides its role in inflammatory and immune response, it is involved in cell proliferation, tumorigenesis, and wound repair (Chatterjee et al., 2014; Pasupuleti et al., 2014). It has also been reported that MIF is a homolog protein of D-dopachrome tautomerase. Similarly, it shows phenyl/pyruvate tautomerase and thiol oxidoreductase activities (Merk et al., 2011).

MIF has been shown to have chaperone-like properties along with all its other functions. The first study conducted by Cherepkova et al. (2006) showed that MIF is

similar to other chaperones such as Hsp70 in that it has a trimeric structure, is a small protein (12 kDa each monomer) (**Figure 1.7**), and a hydrophobic surface. In later studies, the chaperone effect of MIF was shown on SOD1; it has been investigated that MIF prevents the formation of the aggregation of misfolded mutant SOD1s in the cytosol and mitochondria and amyloid-like fibrils from aggregates (Shvil et al., 2018). The mechanism of MIF to prevent misfolding and help to fold SOD1 properly is still unclear and providing insight into the underlying mechanism might be a significant step for developing therapeutics target SOD1.

1.8 The Aim of the Thesis

So far, all X-ray structures of wild-type and mutant SOD1 entered in PDB are obtained from data collected at cryogenic temperatures. Although SOD1 is a stable homodimer protein in its fully mature active form, there are intermediate forms of SOD1 in its maturation process to become a folded protein. Crystallization at low temperature and freezing protein crystals for diffraction data collection provide to see proteins as the most stable form. However, we cannot see more flexible intermediate forms of wild-type SOD1 or conformational changes of mutant SOD1s at cryogenic temperatures. We aimed to determine conformational changes during dimerization of the protein and structural effects of mutations in the SOD1 using X-ray crystallography approaches at ambient temperature. The second aim of this thesis is to solve the structures of VDAC1 and MIF, which are interaction partners of SOD1 and to show the interaction between SOD1 and these proteins with the X-ray crystallography method.

Chapter 2:

MATERIALS AND METHODS

2.1 Plasmid Selection and Design for SOD1, VDAC1 and MIF

pET28a (+) expression vector carrying six histidine tags and thrombin cleavage site was used for overexpression of full-length human $SOD1^{WT}$, $SOD1^{G93A}$, VDAC1 and MIF genes (**Figure 2.1**). The codon-optimized genes were synthesized and inserted into the pET28a (+) vector plasmid by cloning. Genscript, USA, performed cloning the genes into the vector. We provided the following amino acid sequences of those genes for the design of the construct (Histidine-tag and thrombin recognition site indicated with green and red colors, respectively).

SOD1 ^{WT} sequence:

1. MGSSHHHHHHSSGLVPR(thrombin_cut_site)GSHMATKAVCVLKGDGPV QGIINFEQKESNGPVKVWGSIKGLTEGLHGFHVHEFGDNTAGCTSAGPHFNPLS RKHGGPKDEERHVGDLGNVTADKDGVADVSIEDSVISLSGDHCIIGRTLVVHEK ADDLGKGGNEESTKTGNAGSRLACGVIGIAQ

SOD1 ^{G93A} sequence:

MGSSHHHHHHSSGLVPR(thrombin_cut_site)GSHMATKAVCVLKGDGPVQGIINF EQKESNGPVKVWGSIKGLTEGLHGFHVHEFGDNTAGCTSAGPHFNPLSRKHGG PKDEERHVGDLGNVTADKDAVADVSIEDSVISLSGDHCIIGRTLVVHEKADDLG KGGNEESTKTGNAGSRLACGVIGIAQ

VDAC1 sequence:

MGSSHHHHHHSSGLVPR(thrombin_cut_site)GSHMAVPPTYADLGKSARDVFTK GYGFGLIKLDLKTKSENGLEFTSSGSANTETTKVTGSLETKYRWTEYGLTFTEK WNTDNTLGTEITVEDQLARGLKLTFDSSFSPNTGKKNAKIKTGYKREHINLGCD MDFDIAGPSIRGALVLGYEGWLAGYQMNFETAKSRVTQSNFAVGYKTDEFQL HTNVNDGTEFGGSIYQKVNKKLETAVNLAWTAGNSNTRFGIAAKYQIDPDACF SAKVNNSSLIGLGYTQTLKPGIKLTLSALLDGKNVNAGGHKLGLGLEFQA

MIF sequence:

MGSSHHHHHHSSGLVPR(thrombin_cut_site)GSHMPMFIVNTNVPRASVPDGFLS ELTQQLAQATGKPPQYIAVHVVPDQLMAFGGSSEPCALCSLHSIGKIGGAQNRS YSKLLCGLLAERLRISPDRVYINYYDMNAANVGWNNSTFA

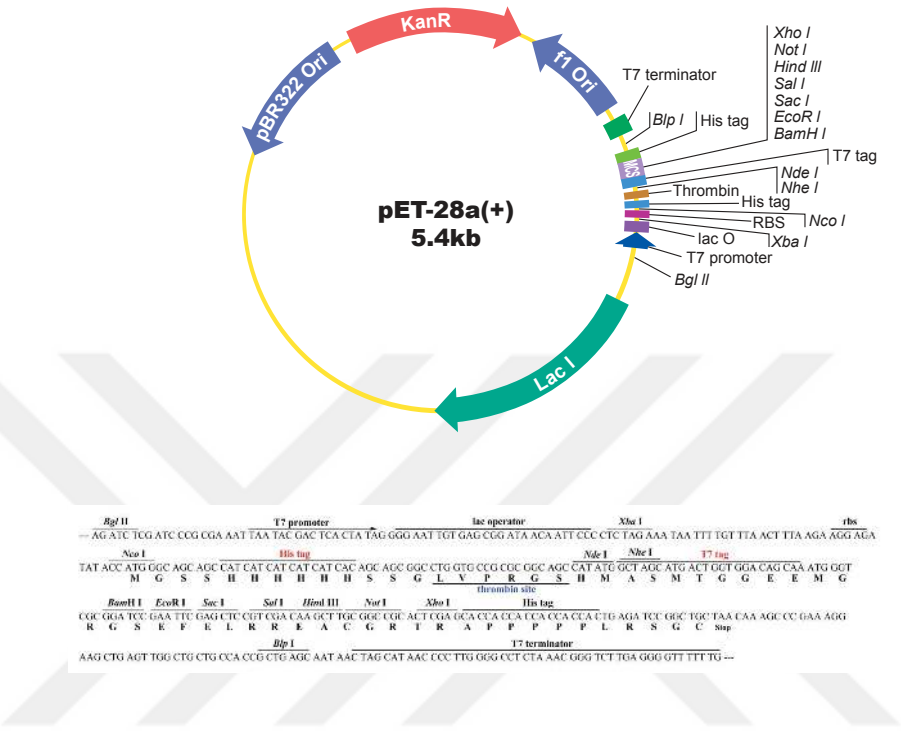

Figure 2.1 Vector map and sequence information of pET-28a (+) plasmid

2.2 Transformation and Bacterial Stock Preparation

The gene constructs cloned to pET-28a (+) were transformed into *E. coli* BL21 Rosetta 2 bacterial strain using heat shock and cultured to LB agar plates with kanamycin and chloramphenicol antibiotics. Then, plates were incubated at 37°C overnight. Colonies were picked from the plate to inoculate in 150 mL LB-Miller broth media (30 g/L) with antibiotics. The cells were grown at 37°C and 110 rpm in the New Brunswick Innova 4430R shaker/incubator overnight. For long-term storage of transformed bacterial culture, 750 µL of the grown cells were mixed with 750 µL 80% glycerol in a 2 m Wuxi NEST Biotechnology cryovials and then placed at -80°C freezer.

2.3 Recombinant Protein Production and Purification

2.3.1. Small Scale Expression of SOD1 ^{WT} and SOD1 ^{G93A}

Samples from glycerol stocks of the cells containing SOD1^{WT} and SOD1 ^{G93A} constructs were inoculated into 150 mL rich LB- Miller (50 g/L) with 50 µg/mL kanamycin and µg/mL chloramphenicol. The cultures were grown overnight in the New Brunswick Innova 4430R shaker/incubator at 37°C and 110 rpm. The cultures were split into three flasks for testing different induction times (24 h, 48h, and 72 h) and induced with 0.4 mM IPTG and 100 µM $ZnCl_2$ at 18°C and 110 rpm in the New Brunswick Innova 4430R incubator.

2.3.2. Small Scale Expression of MIF and VDAC1

A small amount from glycerol stocks of cells transformed with pET-28a(+) containing MIF and VDAC1 genes was inoculated into separate 150 mL standard LB-Miller (30 g/L) supplemented with 50 µg/mL kanamycin and 35 µg/mL chloramphenicol. Cell cultures containing these genes were grown in the New Brunswick Innova 4430R shaker/incubator at 37C and 110 rpm. 20 mL of the grown culture was used for the induction process. Induction was applied with 0.4 mM IPTG at 18°C and 110 rpm.

2.3.3. Protein Purification on the Small Scale (Pull-down Assay)

After overnight induction, cells were transferred to a 50 mL falcon tube and centrifuged at 3500 rpm for 30 min in the Beckman Allegra 15R centrifuge. The supernatant part was discarded, and pellets were put into a -80°C freezer for storage. 20 mL lysis buffer containing 500 mM NaCl, 150 mM Tris pH 7.5, 0.1% Triton X-100 and 5% glycerol was added to the pellet to lyse the cells and pellets sonicated on the ice at 30% amplitude and during the 30s (1s on, 1s off) with Branson W250 Sonifier. After the sonication process, the sample was centrifuged at 15000 rpm for 30 min with the Beckman Avanti J-26S centrifuge. The supernatant of each sample was transferred to another 50 mL falcon tube, and then 500 µL Ni-NTA agarose resin was added to the tube and inverted a couple of times. The mixture was incubated overnight in a 4°C refrigerator. The supernatant containing beads was centrifuged at 1000 rpm for 1 min. The supernatant was discarded without moving the beads at the bottom of the falcon tube. The remaining

beads were incubated on the ice for 30 min with a washing buffer containing 150 mM NaCl and 20 mM Tris-HCl pH 7.5. The washing buffer added beads were centrifuged again at 1000 rpm for 1 min, and the supernatant was discarded. The beads were transferred to a microcentrifuge tube. 1 mL elution buffer containing 150 mM NaCl, 20 mM Tris-HCl pH 7.5 and 250 mM imidazole and proteins bound to resin were eluted by centrifuge at 1000 rpm for 1 min. The expression of each protein was validated by BioRad TGX-mini protean gradient SDS-PAGE.

2.4 Protein Expression and Purification on a Large Scale

2.4.1. Large-Scale Protein Expression and Purification of SOD1 ^{WT} and SOD1 ^{G93A}

Firstly, the stock cells containing SOD1^{WT} and SOD1 ^{G93A} genes were grown overnight in the 150 mL rich LB (50 g/L) supplemented with 50 μg/mL kanamycin and μg/mL chloramphenicol at 30°C and 110 rpm using the New Brunswick Innova 4430R incubator. 150 mL cell culture was added to 4.5 L rich LB w/ same antibiotics and grown at 30C and 110 rpm until OD600 was equal to 0.8. To induce protein production, 0.4 mM IPTG and 100 uM $ZnCl_2$ were mixed with the grown culture and incubated overnight at 20°C and 110 rpm. After overnight incubation, pellets were harvested by centrifugating at 3500 rpm for 45 min in the Beckman Allegra 15R centrifuge. Pellets were stored at -45°C freezer. For the lysis process, a buffer containing 500 mM NaCl, 150 mM Tris pH 7.5, 0.1% Triton X-100 and 5% glycerol were added to the top of the pellets. To make proteins soluble the pellets with the lysis buffer were sonicated at 85% amplitude for 30 s (1s on, 1s off) using Branson W250 Sonifier. The completely resuspended solution after sonication was centrifuged at 35000 rpm for one hour in the Beckman OptimaTM L-80 XP Ultracentrifuge. The supernatant was transferred to a bottle and was ready for loading to the Ni-NTA column.

Purifying the protein from the supernatant sample with nickel affinity chromatography was performed using the QIAGEN Ni-NTA agarose resin column. Firstly, before loading the sample, the column was equilibrated with a loading buffer containing 250 mM NaCl and 25 mM Tris-HCl pH 7.5. After this process, the supernatant was filtered with a 0.44 um membrane filter and then loaded to the Ni-NTA column with 2.5 mL/min flow rate using the AKTA GO FPLC. When the loading step was finished, the column was washed with the buffer containing 250 mM NaCl and 25 mM Tris-HCl

pH 7.5. To get rid of non-specifically bound E. coli proteins, the column was also washed with loading buffer with 25 mM imidazole. After those washing steps, the protein was eluted from the column with elution buffer (250 mM NaCl, 25 mM Tris-HCl and 250 mM imidazole). The eluted protein sample was loaded into 12% TGX mini-protean SDS-PAGE gel to validate purified protein.

2.4.2. Large-Scale Protein Expression and Purification of MIF and VDAC1

For overnight starter culture of the large-scale expression of MIF protein, the stock cell containing the gene was inoculated in 150 mL standard LB (30 g/L) with 50 µg/mL kanamycin and 35 µg/mL chloramphenicol and grown at 37°C and 110 rpm in the New Brunswick Innova 4430R incubator. The culture grown overnight was added to 4.5 L standard LB supplemented with the same concentration of the antibiotics and grown at 37°C and 110 rpm. When OD600 reached 0.8-1.2, protein expression was induced with 0.4 mM IPTG overnight at 18°C and 110 rpm. The purification procedure of MIF was the same as that applied to the $SOD1^{WT}$ and $SOD1^{G93A}$ protein, with the same buffers at pH 8.5. Since VDAC1 is a membrane protein, to purify the protein on-column refolding process was applied.

2.4.3. Refolding of VDAC1

After induction of VDAC1 expression, pellets were collected and lysed with a lysis buffer (Buffer A) containing 500 mM NaCl, 50 mM Tris-HCl pH 7.5, 0.1 Triton-X-100, 5% Glycerol and 25 mM imidazole to get rid of other bacterial proteins. The lysate was centrifuged at 20000 rpm for 30 min in the Beckman OptimaTM L-80 XP Ultracentrifuge. Since VDAC1 was in the pellet, the pellet was collected in this step, not the supernatant. The collected pellet was dissolved overnight on the stirrer with a buffer (Buffer B) containing 8 M Urea, 500 mM NaCl, 20 mM Tris-HCl pH 7.5 and 10%Glycerol. The mixture was centrifuged at 35000 rpm for one hour and the supernatant part was collected in the bottle. For refolding process of VDAC1 protein, the buffer containing 150 mM NaCl and 20 mM Tris-HCl pH 7.5 and 1% Triton-X 100. The protein sample (25 mL) was added to the refolding buffer by dropwise method.

2.5 Reverse Ni-NTA Chromatography

Purified $SOD1^{WT}$, SOD^{G93A} and MIF proteins with the N-terminal hexahistidine tag were cleaved overnight at 4°C by thrombin enzyme to remove the His-tag. SDS-PAGE was performed to validate the cleavage of His-tag. AKTA GO instrument and Ni-NTA agarose resin column were used to collect the protein without His-tag. The protein sample was loaded to the column with 2.5 mL/min flowrate. After loading the sample, the fraction was collected from flow through containing proteins that do not have histidine tag. The bound SOD1 proteins were eluted with the buffer containing 250 mM NaCl, 50 mM Tris-HCl pH 7.5 and 250 mM imidazole. The bound fraction of MIF was collected with the same buffer with pH 8.5. Purified and thrombin cut proteins were aliquoted to 1.5 mL microcentrifuge tubes, frozen with liquid nitrogen and then stored at -80°C freezer.

2.6 Protein Crystallization

To crystallize the purified proteins with and without the His-tag, more than 3000 commercial crystal screen conditions were used. 0,83 µL of protein sample and 0.83 µL crystal screening condition were added to one well of the 72-well Terasaki plate and covered with 16.6 µL paraffin oil using the sitting drop microbatch under the oil method. Crystallization was performed at room temperature for $SOD1^{WT}$ and $SOD1^{G93A}$ samples and 4°C for the MIF protein sample. Each well was checked each week under the light microscope until crystals were formed. Concentrations of the proteins used for crystallization were 4.8 mg/mL, 5.6 mg/mL and 6.7 mg/mL for $SOD1^{WT}$, $SOD1^{G93A}$ and MIF, respectively.

2.7 Diffraction Data Collection and Processing

The diffraction data collection experiments were performed in the Turkish Light Source (XtaLab Synergy-S (Rigaku)) home source X-ray diffractometer consisting of a four-axis Kappa goniometer (omega, kappa, theta and phi), micro-focus X-ray tube and HyPix-Arc 150° detector (Rigaku) (**Figure 2.2**). All parts of data collection were performed at cryogenic and room temperatures. XtalCheck-S plate reader tool was mounted to conduct the experiment at ambient temperature. The plate reader provides a

way to collect data from the Terasaki plate directly. After mounting the XtalCheck-S apparatus, the Terasaki plate with the SOD1 crystals was placed in the plate reader with the appropriate adapter. XtaLab Synergy-S synchronized with CrysAlis Pro software to operate the system and the experiment. All the formed crystals on the three Terasaki plates were scanned. For diffraction scanning of the crystal, the beam intensity was arranged to 10% and one frame was collected with 1s exposure time for each crystal. Diffraction data collection continued with the crystals in the two well of Terasaki plate containing 1 µL Stura Footprint #2-24 + 0.5 µL Additive screen #27 and 1 µL Wizard II #7 + 0.5 µL Additive screen #2 conditions. The omega degree range, which provides to rotate plate reader using the omega axis, was expanded and the exposure time was increased to 60s to collect more frames from the crystals.

Figure 2.2 The picture of XtaLab Synergy-S equipped with HyPix-Arc 150° detector and XtalCheck-S plate reader.
Numbers indicate the hardware parts of the instrument; 1) X-ray tube, 2) four-axis Kappa goniometer, 3) XtalCheck-S plate reader and 4) detector.

CrysAlisPro software was used to process the raw data. Firstly, all the PDB structures are listed to compare their unit cell and space group information. The data reduction process was carried out by manually selecting the desired space group and unit cell for each collected dataset from different crystals. To increase the completeness of the structure data, different diffraction datasets of crystals in the same well with the same space group and similar unit cells were merged. The unit cell parameters were a = 84.60,

b =123.07, c = 153.23, α = 90, β = 90, γ =90 and space group was P 21 21 21 for the merged data. This data is used for phasing and refinement processes.

2.8 The Determination, Refinement, and Visualization of the Three-dimensional Structure

The wild-type apo structure of SOD1 was determined by performing molecular replacement with the PHASER extension of PHENIX software. The twelve monomer copies of structure of SOD1 with Cys57Ala/ Cys146Ala mutations (PDB ID:6FOI) were used as a model to determine the structure with the molecular replacement. The initial rigid-body refinement with the coordinates of the model was performed using the PHENIX.refine extension in the GUI of the PHENIX software. After initial refinement, the TLS parameters and individual coordinates were also refined using PHENIX software. COOT software was used to check and correct the altered side chains and missing water molecules. Cys57Ala and Cys146Ala mutations were also changed with the original residues in COOT. Since the electron density maps of zinc ions were not observed in both chains, zinc atoms were removed from the structure. After all refinements, the Ramachandran statistics (favored/allowed/outliers) of the structure were 85.87, 12.53 and 1.60 %, respectively. The R_{work} and R_{free} values were 0.35 and 0.40. The visualization of the three-dimensional structure of $SOD1^{WT}$ and structural alignments were performed using PyMOL.

Chapter 3:
RESULTS

3.1 Large Scale Purification Results

3.1.1. SDS-PAGE Results of SOD1^{WT} Protein

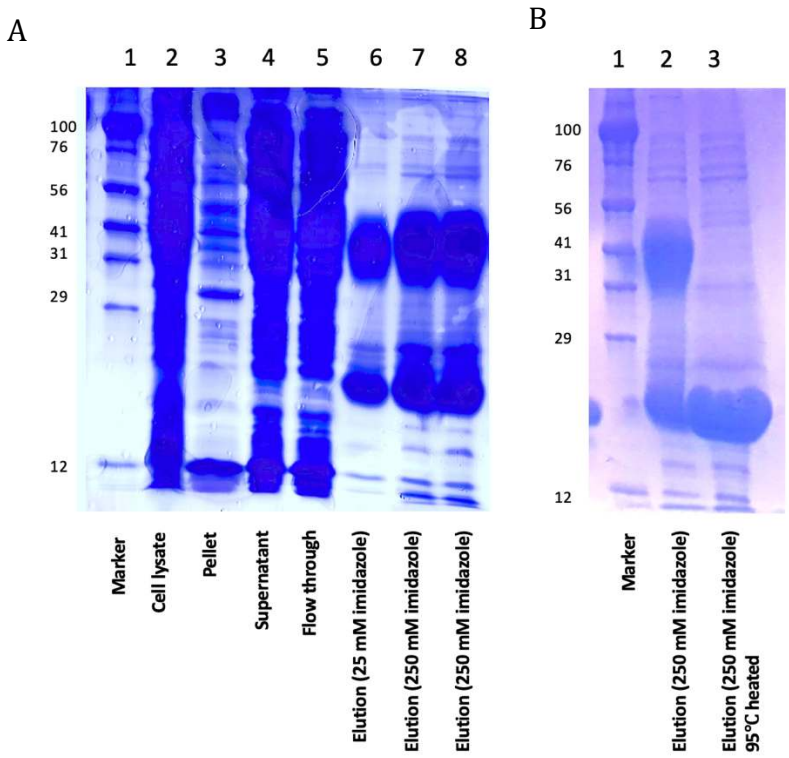

Figure 3.1 SDS-PAGE electrophoresis results of purified SOD1 protein
A) The first lane is the KUYBIIG-M ladder. The second lane shows the whole cell lysate after induction. The third and fourth lanes represent the pellet and supernatant part of the whole cell lysate after centrifuge. The fifth lane is flow through sample that includes non-bound proteins. The sixth, seventh and eighth lanes are elution samples with 25 mM, 250 mM, and 250 mM imidazole containing elution buffer. B) Marker, Non-heated and heated (95 °C) elution samples are represented in lanes 1, 2 and 3, respectively.

The purified his-tagged SOD1 protein samples were obtained by performing Ni-NTA affinity chromatography and then they were visualized with SDS-PAGE and Coomassie Blue dying techniques (**Figure 3.1**). SOD1 is a homodimer protein with 32 kDa molecular weight, and each monomer's molecular size is 16 kDa. Two possible bands can be observed in the SDS-PAGE gel. In the monomer form of the protein, the band is expected between 12 kDa and 29 kDa bands of the KUYBIIG-M marker. Otherwise, the band of homodimer SOD1 must be between 31 kDa and 41 kDa. To see the expression and solubility of the protein after induction whole cell lysate, pellet and supernatant

(Lanes A-2, A-3 and A-4) were loaded into the gel. After induction sample, supernatant and flow through were dyed too much and the results of those lanes are not readable (Lanes 2A, 4A and 5A). According to previous studies wild-type SOD1 is produced as a soluble protein in E.Coli BL21 strains. In this experiment, the protein was almost totally soluble after the production of $SOD1^{WT}$ in E. Coli BL21 (Rosetta 2) and purification. In the pellet sample, there was a band between 29 and 31 kDa belonging to a protein of Rosetta 2 (Lane A-3). It has also been observed in the pellet samples of other expression experiments performed in the KUYBIIG-M laboratory. Elution samples were collected with 25 mM imidazole and 250 mM imidazole-containing buffer (Lanes A-6, A-7 and A-8). Two bands of monomer (16 kDa) and dimer (32 kDa) form were observed in these three samples. To make sure whether the bigger band is a dimer or not, the elution sample was heated to 95°C and then loaded to SDS-PAGE gel. The two bands were seen in one band indicating monomer (Lane B-3).

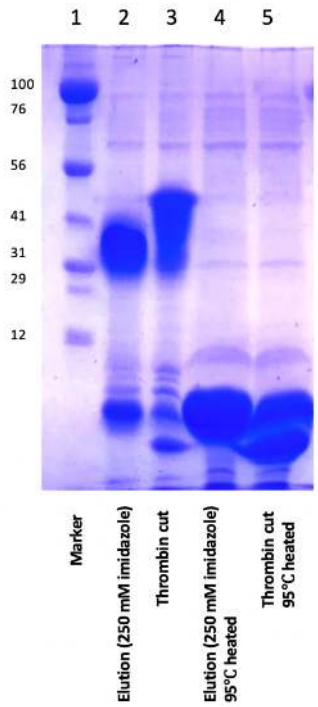

Figure 3.2 Results of histidine tag removal by thrombin cut
As usual first lane is the marker. Lane 2 and 3 represent elution and thrombin cut results without heating. Lane 4 and 5 indicate heated (95 °C) elution and thrombin cut samples.

After the purification experiment, His-tag of half of the protein was removed from the protein by using the thrombin enzyme (**Figure 3.2**). The elution and thrombin-added elution samples were loaded to gel after an overnight cleavage reaction. The unheated

and heated (95°C) samples of both with his-tag and expected without His-tag samples were loaded into SDS-PAGE gel (Lane 2-5). Interestingly, when the protein was cleaved by the thrombin enzyme, the protein revealed a heterogeneous conformational profile (Lane 3). The thrombin cut sample was heated to 95°C to make sure that all the different bands belong to SOD1 and whether the protein was totally cut or not. As is shown in **Figure 3.2**, there was a half shift in the heated sample (Lane 5). Since the shift was not seen clearly in the gel, the thrombin cleavage reaction was continued for one more night (18 h) to make the protein ready to set up crystallization.

3.1.2. SDS-PAGE Results of SOD1^{G93A} Protein

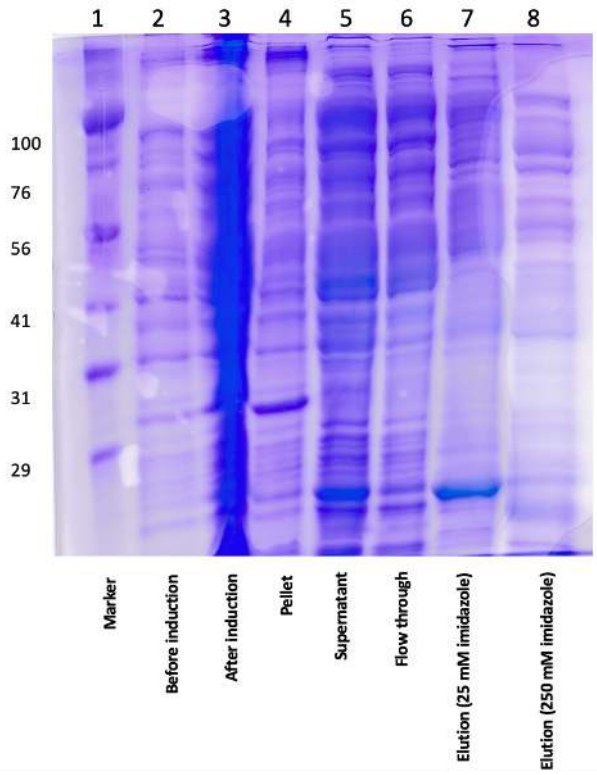

Figure 3.3 SDS-PAGE results of purified SOD1^{G93A} mutant form
The first lane is the marker. The second and third lanes are before and after induction of whole cell lysate samples. Lanes 4 and 5 represent pellet and supernatant samples after lysis. Lane 6 is flow through. The last two lanes (7 and 8) are elution samples with 25 mM imidazole and 250 mM imidazole, respectively.

The same procedure with the wild-type SOD1 was applied to purify the SOD1^{G93A} protein. To compare the expression level of the protein before and after induction samples were loaded to lanes 2 and 3 of the gel (**Figure 3.3**). Since the after induction sample was overloaded into the gel, we cannot decide the difference in expression levels between before and after induction. After sonication and centrifuge processes, pellet and

supernatant were loaded to lanes 4 and 5 to check the solubility of the protein. The pellet sample had a band between 29 and 31 kDa. However, this band was one of the proteins of the Rosetta 2 bacterial strain. The supernatant sample has a thicker band than the other bands of the bacteria (Lane 5). This band between 12 and 29 kDa indicates the monomer form of the protein. The same band was also shown in elution with 25 mM imidazole sample, but there was no SOD1 band in the elution sample with 250 mM imidazole. After purification, the thrombin enzyme was used to remove His-tag from the protein sample. The reverse Ni-NTA chromatography method removed His-tag and cleaned background non-specific bound proteins after three days of thrombin cut (**Figure 3.4**). Three flow-through samples were collected to see unbound proteins and the SOD1 protein was in the third flow-through sample (Lane 4-6). The third flow through sample has a clear band of $SOD1^{G93A}$ that was used to set up crystallization (Lane 6).

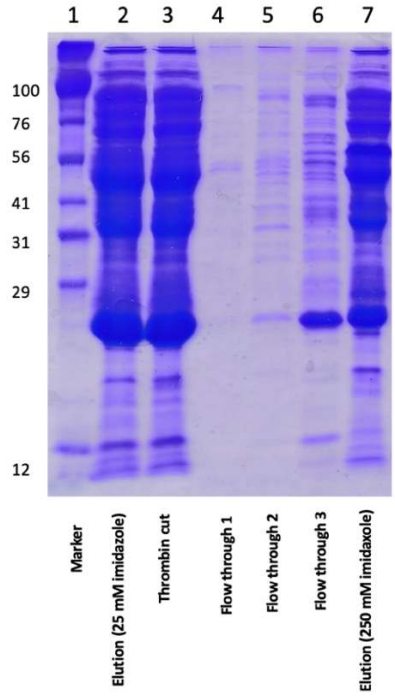

Figure 3.4 Reverse Ni-NTA chromatography results of $SOD1^{G93A}$
The first lane represents the KUYBIIG-M protein marker. The elution sample from the purification experiment was shown in lane 2. Lane 3 indicates three days thrombin cut sample. The following three lanes (4, 5, 6) are flow-through samples collected during Ni-NTA chromatography. The last lane shows the elution sample with 250 mM imidazole.

3.1.3. SDS-PAGE Results of MIF

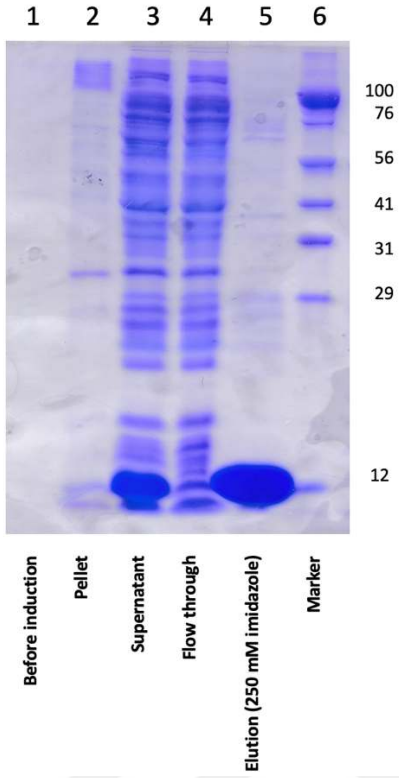

Figure 3.5 SDS -PAGE results of large-scale purification of MIF
The first lane shows before the induction sample. After induction, the centrifuged pellet and supernatant samples were presented in lanes 2 and 3. Flow-through and elution samples of the purification process were shown in lanes 4 and 5. The last lane represents the marker.

The following process of the purification of the protein was conducted by Ni-NTA affinity chromatography and the SDS-PAGE was used to validate the results of purification (**Figure 3.5**). The estimated monomer molecular weight of the MIF protein is 12 kDa. After sonication and centrifugation, the protein was seen in the supernatant sample as soluble compared to the pellet sample (Lane 2 and 3). No significant band indicated 12 kDa in lane 4 containing the flow-through sample. It shows that most of the protein obtained was bound to the Ni-NTA column. The all-bound protein was observed in the elution with 250 mM imidazole sample as a clear band (Lane 5).

3.1.4. SDS-PAGE Results of Refolding VDAC1 Protein

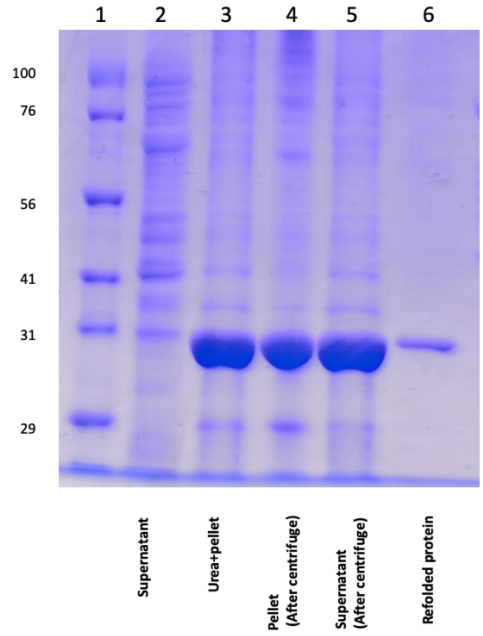

Figure 3.6 Refolding results of VDAC1 protein
The first lane is the marker. Supernatant sample of centrifugation after lysis is shown at 2nd lane. Lane 3 represents the dissolved pellet sample. Pellet and supernatant samples of centrifuged dissolved protein are presented at lanes 4 and 5. At lane 6, refolded sample with dropwise method in washing buffer + 1% Triton X-100 detergent.

After the lysis process with sonication and ultracentrifugation at 20.000 rpm, the supernatant and pellet samples were collected. Since the VDAC1 protein is a human mitochondrial membrane protein with a 32 kDa expected size., expressed soluble proteins of E. coli were observed in the supernatant sample and the band of the VDAC1 was in the pellet. To make the membrane protein soluble, the pellet sample was dissolved in the refolding buffer containing 8 M Urea, 500 mM NaCl, 20 mM Tris-HCl pH 7.5 and 10%Glycerol. This dissolved pellet sample was loaded to the gel and the thick band in the third lane indicates the VDAC1 protein. After totally dissolving the pellet, the sample was centrifuged again at 20.000 rpm speed. Supernatant and pellet samples were loaded to the gel to show the solubility of the protein after the unfolding process (Lanes 4 and 5). More than half of the protein was successfully passed into the solution. The unfolded soluble 25 mL protein was refolded in the 500 mL buffer containing 1% Triton-X 100 detergent (Lane 6). There was no precipitation issue with the refolded protein (**Figure 3.6**).

3.2 Crystallization Results of SOD1

The crystallization experiment was conducted with 4.8 mg/mL SOD^{WT} protein concentration. Approximately 3500 crystal screen conditions were used to screen and find the best crystal condition for the protein. Crystals were obtained from different conditions. The following crystals with six different crystal screen conditions were chosen as the best candidates for diffraction data collection. All these crystals were formed at room temperature (**Figure 3.7**). The conditions were Wizard III #20, Stura footprint #2-24, Peg Rx II #20, Wizard I #1, Wizard I #41 and Wizard II #7. The names and ingredients of the conditions are listed in **Table 3.1**.

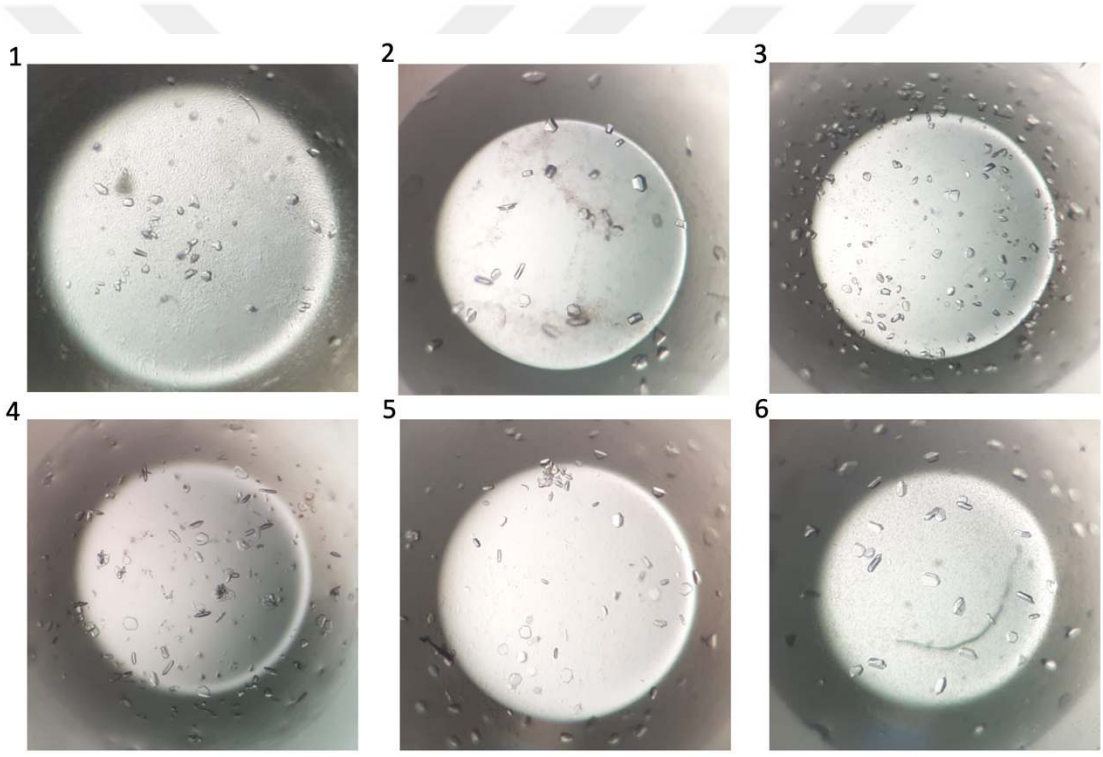

Figure 3.7 The light microscope pictures of $SOD1^{WT}$ protein with His-tag observed after crystallization experiment at room temperature
The numbers are indicated in Table 3.1.

Table 3.1 Screening conditions of obtained crystals from His-tagged $SOD1^{WT}$.

#	Condition name	Precipitant	Buffer	Salt
1	Wizard III #20	10% (w/v) PEG 6000	0.1 M HEPES/ Sodium hydroxide pH 7.0	-
2	Stura footprint #2-24	27% (w/v) PEG 10000	0.1 M Ammonium acetate pH 4.5	-
3	Peg Rx II #20	24% w/v PEG monomethyl ether 2,000	0.1 M Sodium acetate trihydrate pH 4.5	-0.02 M Nickel (II) chloride hexahydrate -0.02 M Magnesium chloride hexahydrate -0.02 M Cadmium chloride hydrate
4	Wizard I #1	20% (w/v) PEG 8000	0.1 M CHES/ Sodium hydroxide pH 9.5	-
5	Wizard I #41	30% (w/v) PEG 3000	0.1 M CHES/ Sodium hydroxide pH 9.5	-
6	Wizard II #7	30% (w/v) PEG 3000	0.1 M Tris base/ Hydrochloric acid pH 7.0	200 mM Sodium chloride

The obtained protein crystals were picked, frozen and then kept cool with a cooling system to collect data at cryogenic temperature (100 K). Different exposure times, resolution limits and beam intensity values were chosen to collect data that we can process, but they showed no diffraction or weak diffraction profile. Crystals were so tiny to collect data and needed to be optimized to get bigger and good-shape crystals. CryoPro (Hampton), Additive screen I and II crystal screen conditions sets were used to optimize crystals. 0.5 µL of each condition was added to 1 µL protein and 1 µL crystal condition that the protein crystal was formed and covered with paraffin oil. The bigger crystals with sharper ends were obtained in the following crystal conditions; 1 µL Stura Footprint #2-24 + 0.5 µL Additive screen #27 and 1 µL Wizard II #7 + 0.5 µL Additive screen #2 (**Figure3.8**). These two crystals were used for diffraction data collection of SOD1 with the XtalCheck-S plate reader tool.

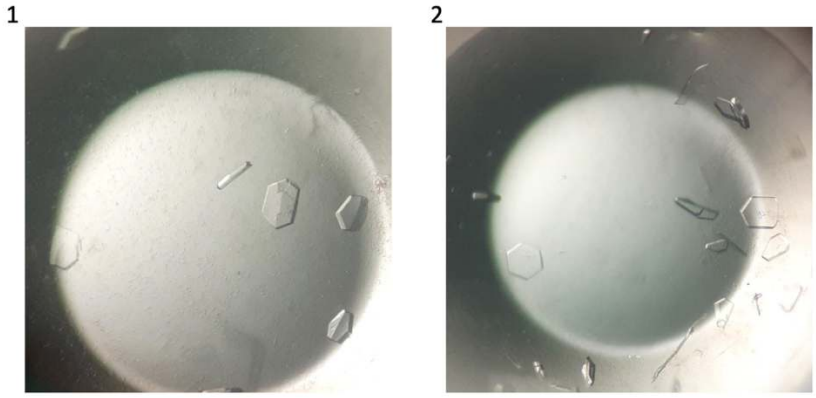

Figure 3.8 The microscope images of SOD1^{WT} with His-tag protein crystals obtained after optimization with additive screens
First image shows crystals formed in 1 µL Stura Footprint #2-24 + 0.5 µL Additive screen #27, second one represents crystals with 1 µL Wizard II #7 + 0.5 µL Additive screen #2 conditions.

The crystallization process was also applied for SOD1^{WT} and SOD1^{G93A} without His-tag and protein crystals of both proteins were observed in the wells (**Figure 3.9**). Crystal screening condition names and ingredients are indicated in **Table 3.2**. We also tried to collect data from these crystals at cryogenic temperatures. However, we observed that only the weak diffractions could not be processed.

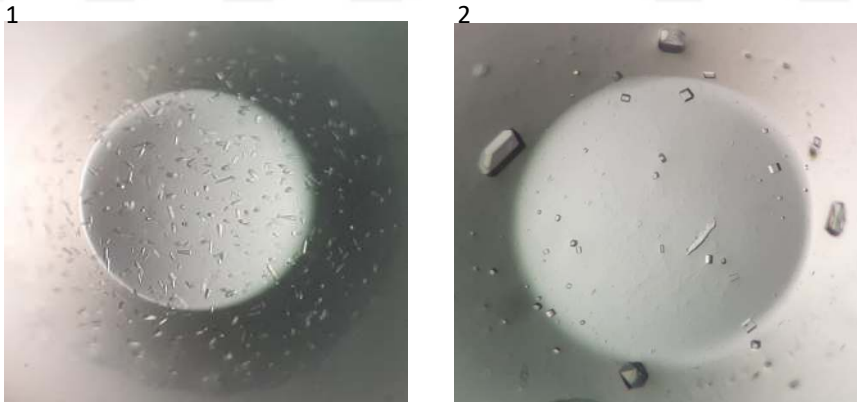

Figure 3.9 The pictures of crystals obtained from SOD1^{WT} and ^{G93A} w/o His-tag
SOD1^{WT} w/o His-tag with Crystal Screen Cryo I #13 condition and 2) SOD1^{G93A} w/o His-tag in Crystal Screen I #8 condition.

Table 3.2 Screening conditions of obtained crystals from SOD1^{WT} and SOD1^{G93A} w/o His-tag.

#	**Condition name**	**Precipitant**	**Buffer**	**Salt**
1	Crystal Screen Cryo I #13	30% v/v Polyethylene glycol 400	0.1 M TRIS hydrochloride pH 8.5	0.2 M Sodium citrate tribasic dihydrate
2	Crystal Screen I #8	30% v/v 2-Propanol	0.1 M Sodium cacodylate trihydrate pH 6.5	0.2 M Sodium citrate tribasic dihydrate

3.3 Diffraction Data

The crystals are indicated in **Figure 3.7.** and **Table 2.1.** were used to obtain the diffraction data from the Turkish Light Source. The first diffraction data collection experiment was performed with cooling samples with liquid nitrogen at 100 K. We could not collect strong diffraction data from all the crystals, only weak diffractions or no diffraction were observed During the experiment at cryogenic temperatures. One example of weak diffraction data is shown in **Figure 3.10.**

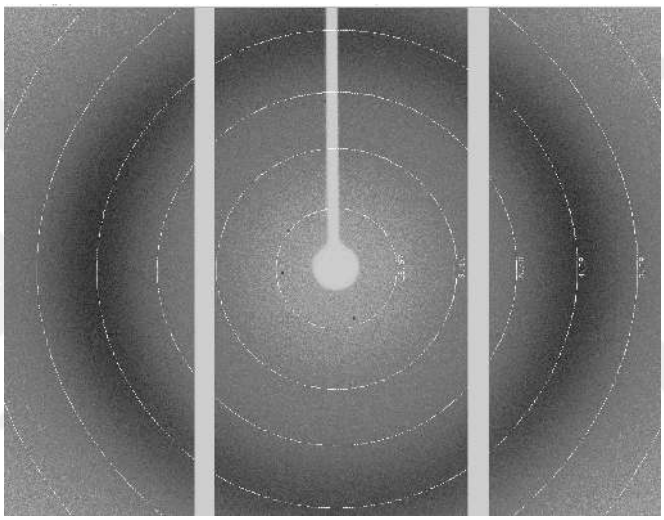

Figure 3.10 Diffraction data of SOD1 collected from Turkish Light Source at cryogenic temperature (100 K)

To optimize the shape, volume and quality of the crystals, 1 µL Stura Footprint #2-24 + 0.5 ul Additive screen #27 and 1 µL Wizard II #7 + 0.5 µL Additive screen #2 crystal screening conditions mixed with 1 µL protein sample. The crystals obtained after optimization were used for another diffraction data collection experiment using the XtalCheck-S plate reader instrument of Turkish Light Source (XtaLab Synergy-S, Rigaku) at ambient temperature. Sixteen different screening experiments with the well containing 1 µL Wizard II #7 + 0.5 µL Additive screen #2 conditions were performed by sending an X-ray beam directly to the well at ambient temperature. Three different diffraction datasets were collected from the crystals obtained under these conditions. One of the diffraction images is represented in **Figure 3.11**.

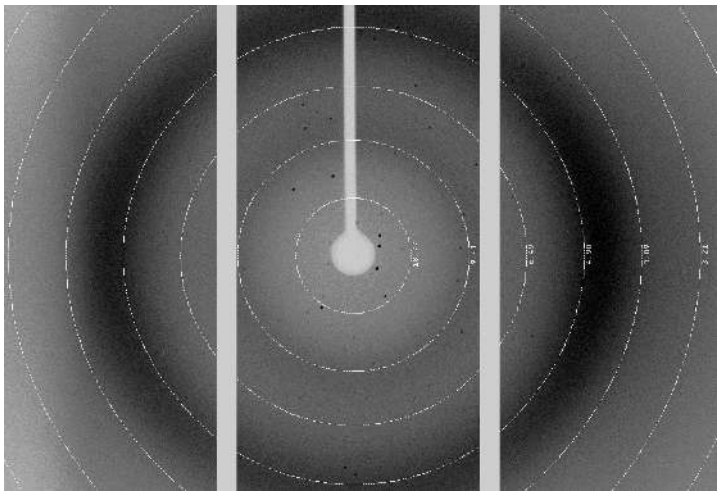

Figure 3.11 Diffraction data of SOD1 collected from Turkish Light Source at ambient temperature with XtalCheck-S plate reader

3.4 The Apo Structure of SOD1 at Ambient Temperature

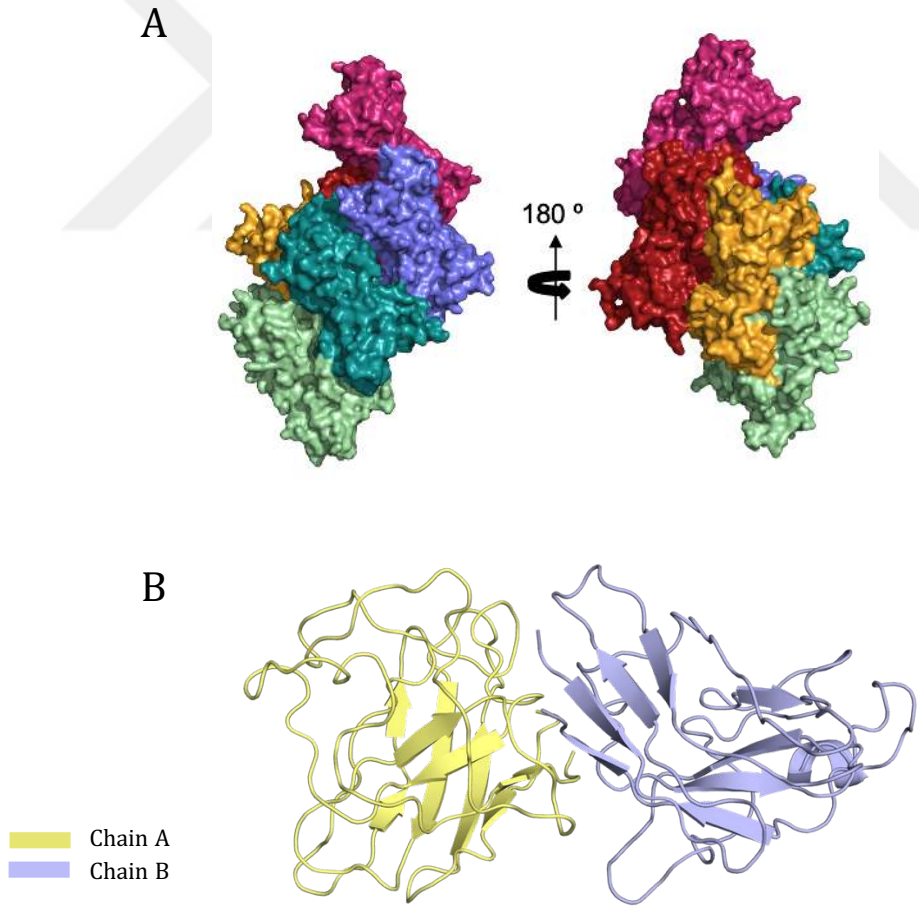

Figure 3.12 The apo X-ray structure of SOD1^{WT} protein at ambient temperature
A) Obtained Hexa-dimer structure of apo-SOD1. B) Chain A and chain B of the structure were represented with pale yellow and light blue, respectively.

After molecular replacement and refinement processes, we determined the metal-free hexa-dimeric structure of SOD1 at ambient temperature with 4.00 Å resolution, P 21 21 21 space group symmetry with R_{free}: 0.40 and R_{work}: 0.35 (**Figure 3.12**). Chain A and chain B of this structure was used to show the dimeric properties of the structure. The detailed information about the statistics of X-ray crystallography is shown in **Table 3.3.** Each monomer has 153 amino acid residues without Cu^{2+} and Zn^{2+} metal ions in the structure. Both monomers have a beta-barrel motif and an alpha-helix in our structure.

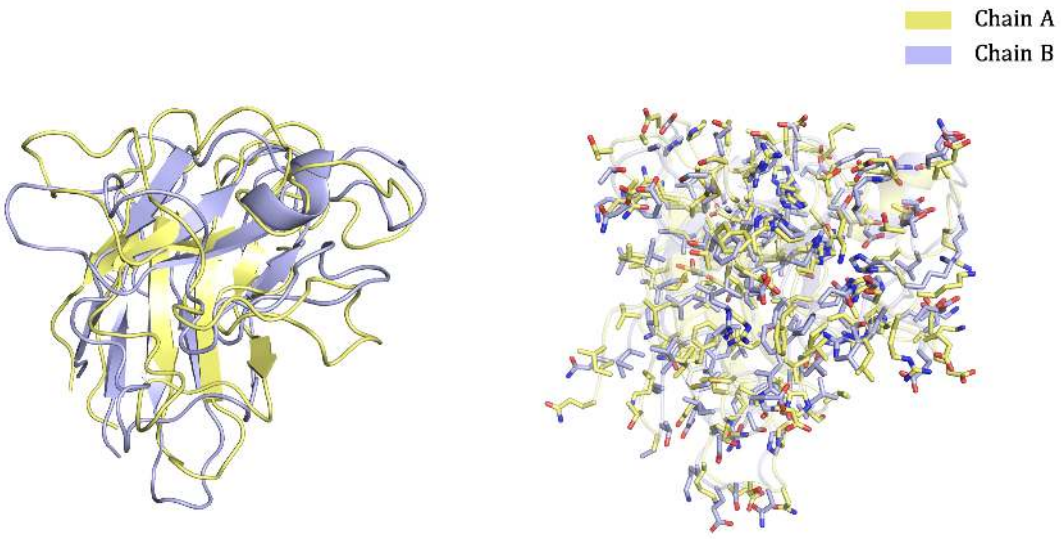

Figure 3.13 The superposition of two monomers of the newly revealed structure of wild-type SOD1 protein
Cartoon (Left) and stick (Right) representations of comparison. Chains were colored pale yellow (chain A) and light blue (chain B).

Although SOD1 is usually a homo-dimer protein, structural changes were observed between the two chains of the apo structure we obtained. These two monomers were superimposed on each other to compare overall structural differences with structural alignment in PyMOL (**Figure 3.13**). 'align' option was used for the alignment of two monomers. C-alpha alignment was applied to 46-146 residues of each monomer. The RMSD value obtained after alignment was 1.724 Å. This value is higher than expected for the homodimer structure.

3.4.1. Active Site Comparison of Chain A and B of the Apo Structure of Wild-type SOD1

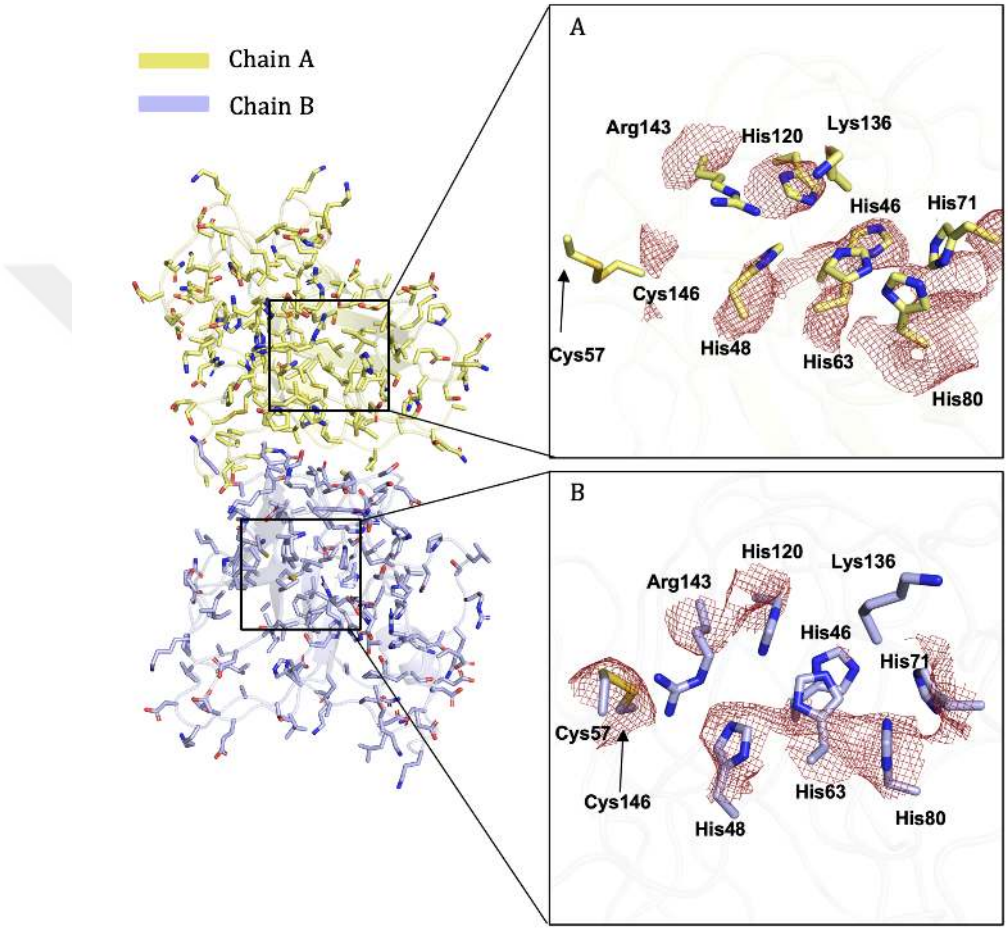

Figure 3.14 Representation of the active site of A and B chains of the ambient temperature SOD1 structure
Active site residues of chain A (A) and chain B (B) were shown in pale yellow and light blue colors, respectively. *2Fo*- Fc simulated omit map was colored by firebrick mesh.

The residues in the active site of SOD1 allow the binding of Cu^{2+} ions to initiate the reaction of enzymatic activity and Zn^{2+} binding and disulfide bond formation stabilizes the structure to provide the environment for the reaction. His63, His71, and His80 residues coordinately bind to zinc and His46, His48, His63 and His120 are copper-binding residues. In addition to metal-binding residues, two positively charged residues (Lys136 and Arg143) are located in the electrostatic loop. These residues are involved in directing O_2^- to the active site. In this region, two cysteine residues (Cys57 and Cys146) form an intra-subunit disulfide bond. In order to show structural changes in the active site

residues between two chains of the structure we obtained, Chain A and Chain B were compared separately with electron density maps of residues. Cys57, Cys146 His71, His80, Lys136 and Arg143 residues of chain A and His46, His120, Lys136 and Arg143 of chain B have lower electron density compared to other active site residues (**Figure 3.14**). Since others have lower electron densities, His46, His48, His63 and His120 of chain A and Cys57, Cys146, His48, His63, His71 and His80 of chain B were used to compare active site residues of chain A and chain B with other known structures of SOD1. The superposition was performed using PyMOL 'align' option for 46-146 residues with C-alpha alignment. The RMSD value is 0.350 Å for the alignment.

3.5. Comparisons of Obtained Apo SOD1^{WT} with Identified PDB Structures of SOD1

3.5.1. Superposition of Dimer and Monomer Structures of Obtained Apo SOD1^{WT} with Other Structures

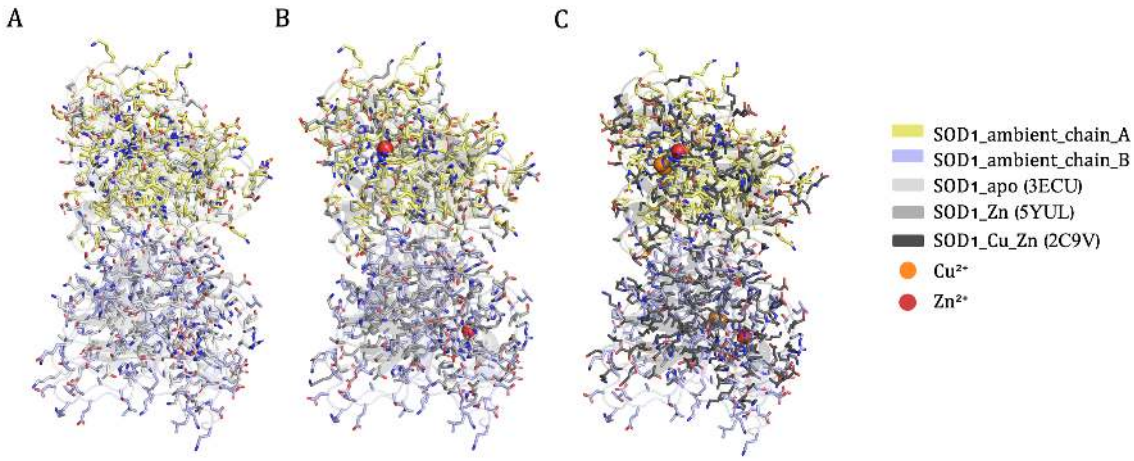

Figure 3.15 The comparison of the dimeric structure of apo SOD1^{WT} at ambient temperature with other SOD1 structures
A) apo (PDB ID: 3ECU), B) Zn^{2+}-bound (PDB ID: 5YUL) and C) Cu^{2+} and Zn^{2+}-bound structures (PDB ID: 2C9V) at cryogenic temperature.

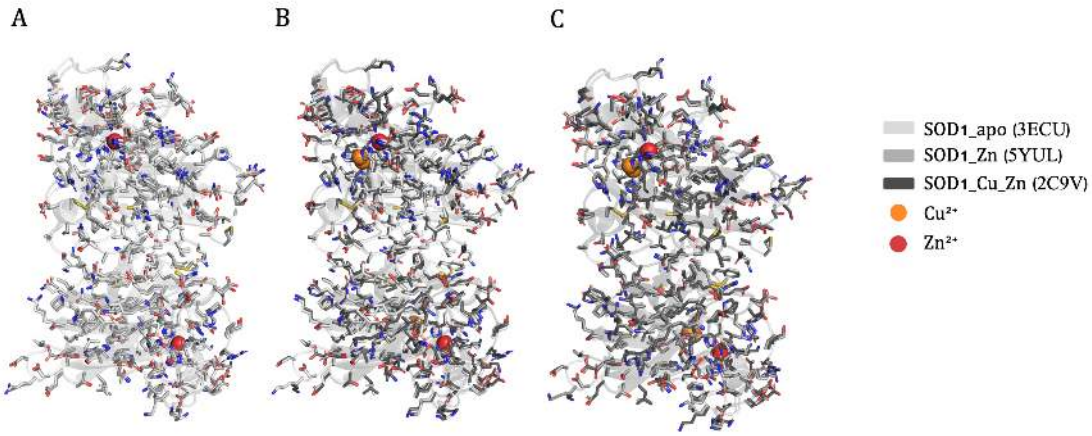

Figure 3.16 The comparison of the known dimeric structures of SOD1
A) 3ECU-5YUL, B) 3ECU-2C9V and C) 5YUL-2C9V comparisons.

The structural differences between apo $SOD1^{WT}$ at ambient temperature and previously identified cryogenic structures of $SOD1^{WT}$ protein were analyzed using structural alignment (**Figure 3.15**). Apo (PDB ID: 3ECU), zinc-bound (PDB ID: 5YUL) and copper and zinc-bound (PDB ID: 2C9V) structures were used to compare with apo $S0D1^{WT}$ structure at ambient temperature. The RMSD values are 3.70 Å for 3ECU, 3.47 Å for 5YUL and 3.25 Å for 2C9V. Although all RMSD values were higher than expected, the structure showing the most similarity to the apo structure was 2C9V. We also superposed the known structures of SOD1 each other. According to alignment results, the RMSD values were 0.53 Å, 0.42 Å and 0.27 Å for 3ECU-5YUL, 3ECU-2C9V and 5YUL-2C9V comparisons, respectively (**Figure 3.16**).

.

3.5.2. Comparison of the Dimer Interface of Apo SOD1^{WT} with Copper and Zinc-bound SOD1^{WT}

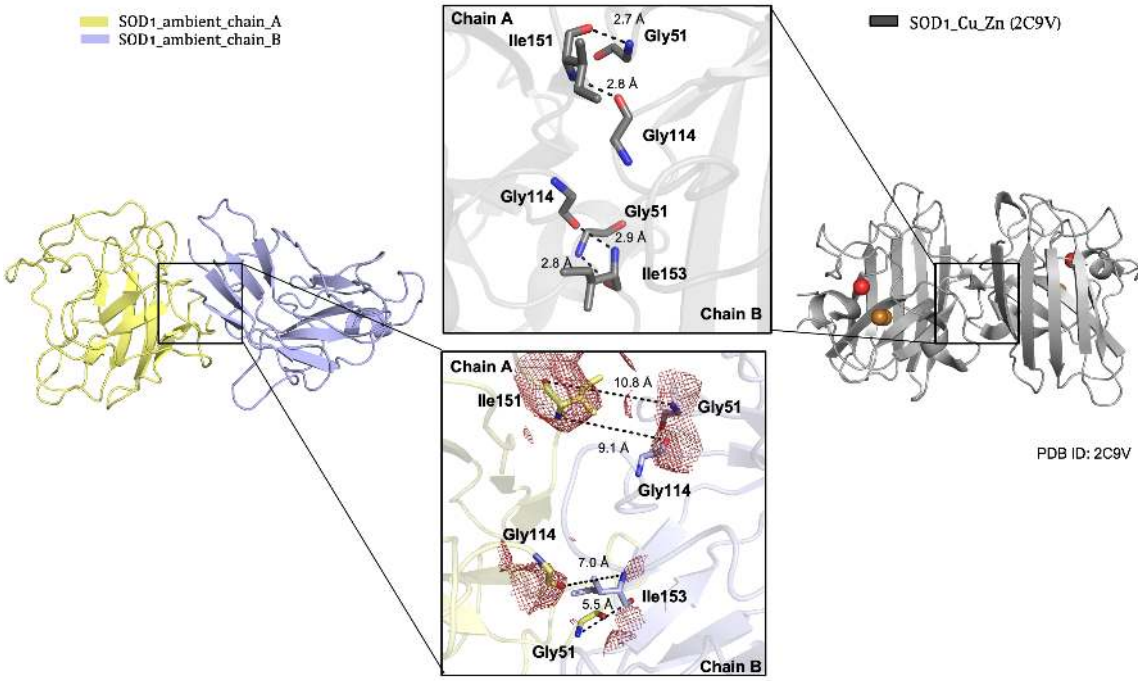

Figure 3.17 The comparison of hydrogen bonding at the dimeric interface of SOD1^{WT}_ambient with the copper and zinc-bound structure (2C9V)

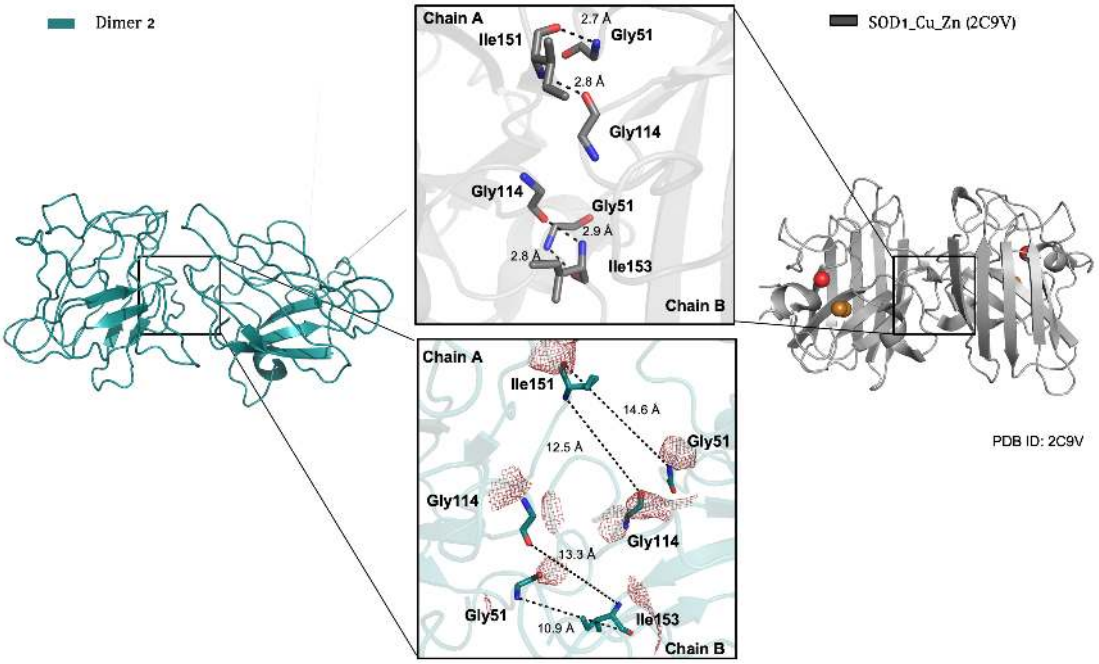

Figure 3.18 The comparison of hydrogen bonding at the dimeric interface of 2nd dimer of SOD1^{WT}_ambient with the copper and zinc-bound structure (2C9V)

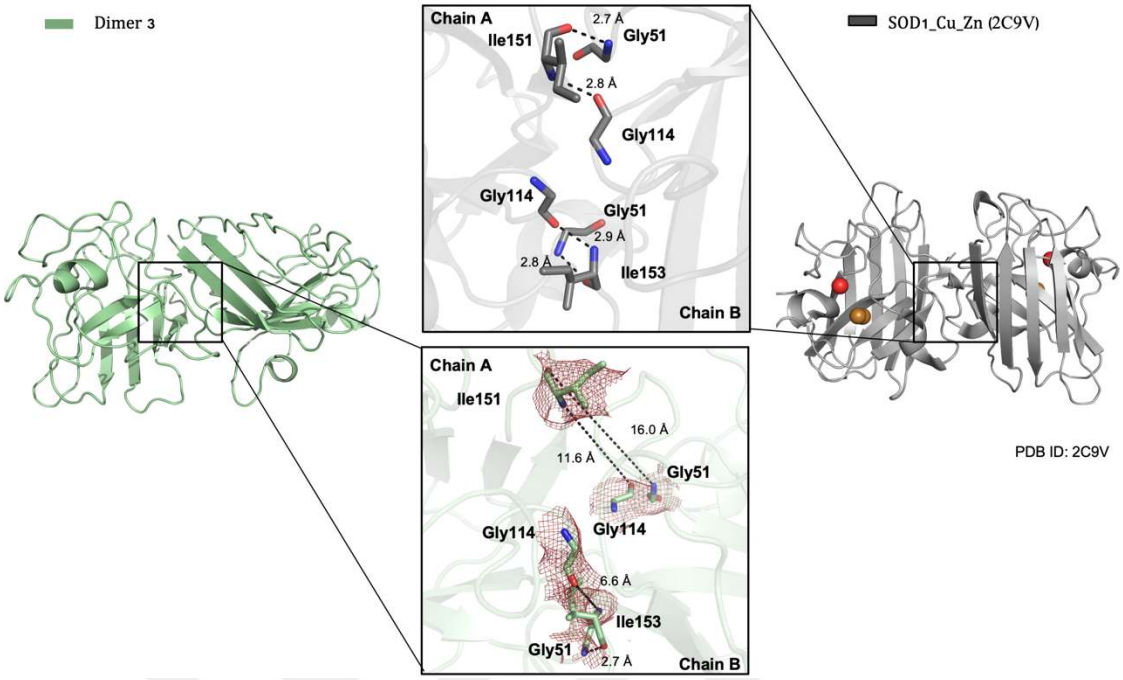

Figure 3.19 The comparison of hydrogen bonding at the dimeric interface of 3rd dimer of SOD1^{WT}_ambient with the copper and zinc-bound structure (2C9V)

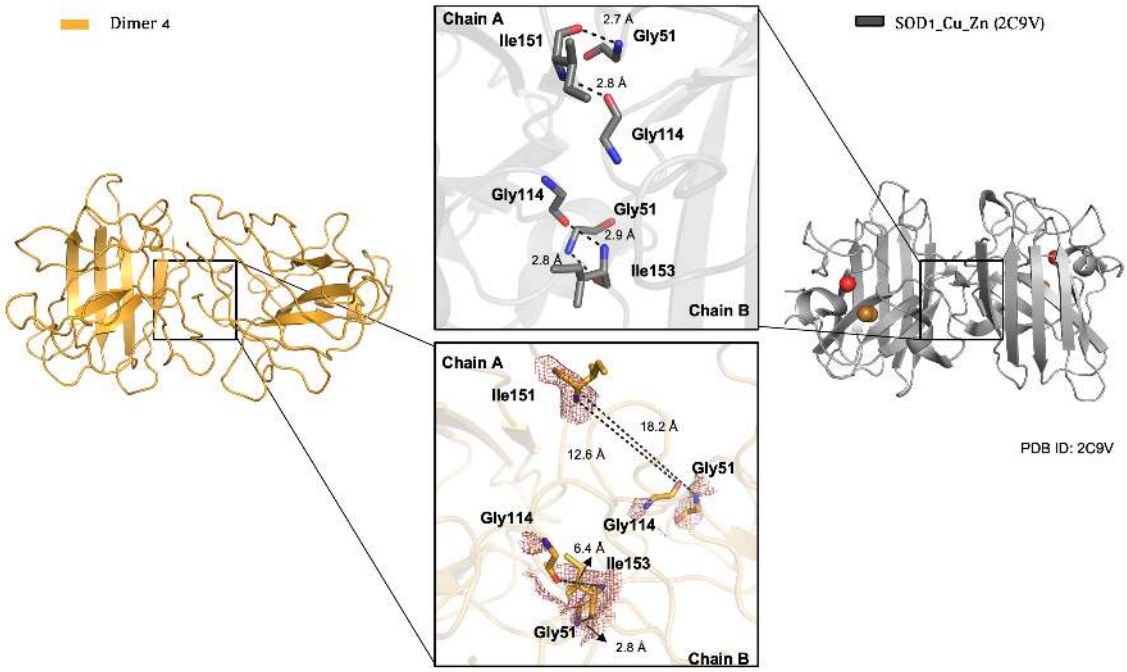

Figure 3.20 The comparison of hydrogen bonding at the dimeric interface of fourth dimer of SOD1^{WT}_ambient with the copper and zinc-bound structure (2C9V)

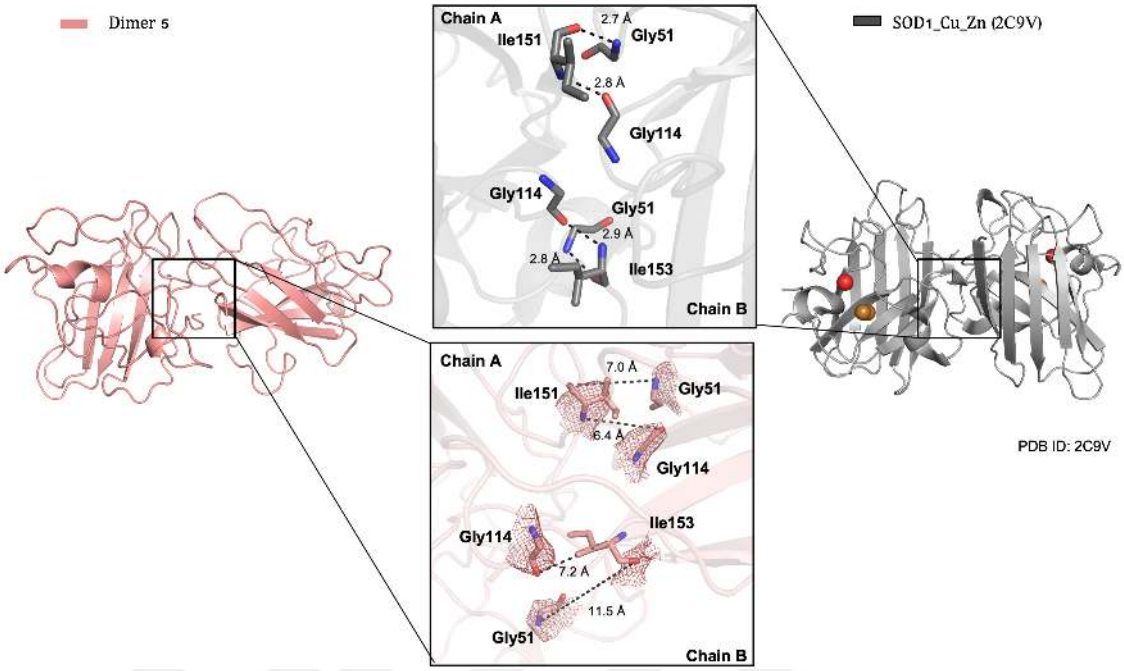

Figure 3.21 The comparison of hydrogen bonding at the dimeric interface of fifth dimer of SOD1^{WT}_ambient with the copper and zinc-bound structure (2C9V)

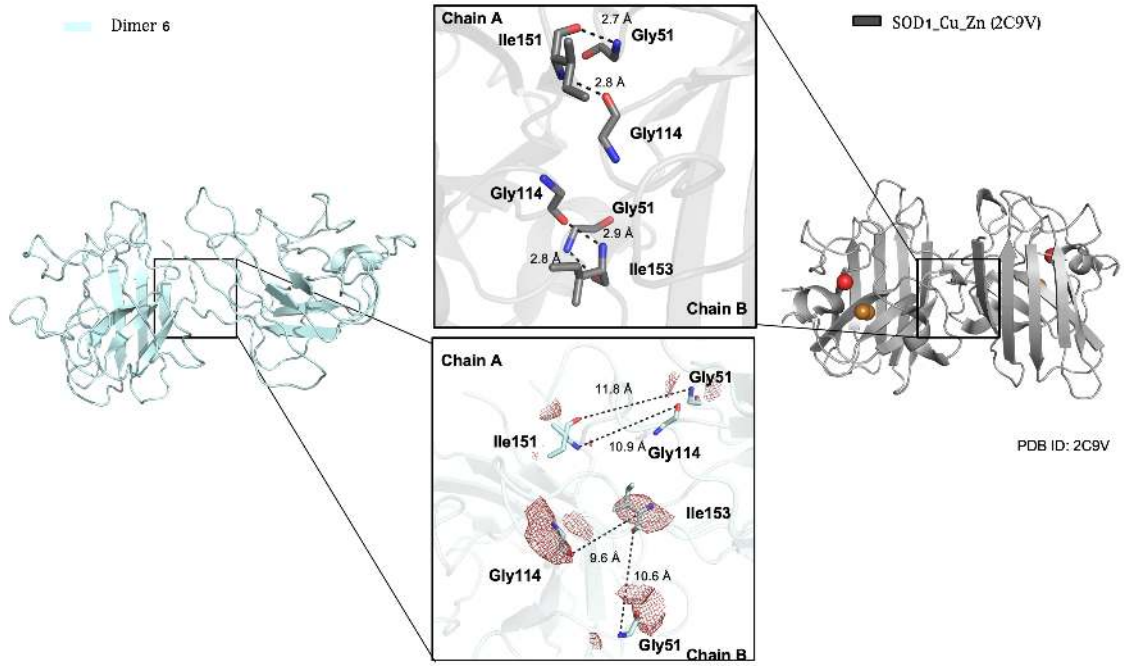

Figure 3.22 The comparison of hydrogen bonding at the dimeric interface of sixth dimer of SOD1^{WT}_ambient with the copper and zinc-bound structure (2C9V)

Non-covalent interactions (hydrogen bonds between two chains and hydrophobic interactions) in the protein's dimeric interface are crucial for stabilizing the dimeric structure. Disruption of those interactions may cause exposure to the hydrophobic

interface and aggregation of the protein. The residues involving the dimeric interface interaction are 50-53, 114, 148 and 150-153 at the C-terminus of both chains. The main interactions that provide stabilization of the dimer are Ile151O (chain A) - Gly51N (chain B), Ile151N (chain A) – Gly114O (chain B), Gly51N (chain A) – Ile151O (chain B) and Gly114O (chain A) – Ile151N (chain B) hydrogen bonds. To check the hydrogen bond formation between chain A and chain B of the new apo structure of $SOD1^{WT}$ structure, the dimeric interface was compared with the stable structure at high resolution (1.07 Å) of copper and zinc-bound $SOD1^{WT}$ (PDB ID: 2C9V) (**Figure 3.17**). In the model used for comparison, the distances for Ile151N (chain A) – Ile114O (chain B) and Gly51N (chain A) – Ile151O (chain B) are 2.8 Å. The hydrogen bonds of Ile151O (chain A) - Gly51N (chain B) and Gly114O (chain A) – Ile151N (chain B) were formed with 2.7 Å and 2.9 Å distances, respectively. None of the hydrogen bonds were formed in the dimer interface of our structure. The distances of Ile151O (chain A) - Gly51N (chain B), Ile151N (chain A) – Gly114O (chain B), Gly51N (chain A) – Ile151O (chain B) and Gly114O (chain A) – Ile151N (chain B) were 10.8 Å, 9.1 Å, 5.5 Å and 7.0 Å respectively. We also compared the dimeric interface of other five dimers of the newly determined structure with 2C9V to understand the differences between the six dimers of our structure. The distances were indicated in the **Figure 3.18, 3.19, 3.20, 3.21 & 3.22**. Only hydrogen bonds between Ile151 (chain B) and Gly51 (chain A) of third and fourth dimers were formed with 2.7 and 2.8 Å, respectively (**Figure 3.19 & 3.20**).

3.5.3. Comparison of the Active Site of New Wild-type SOD1 with the Previously Identified Structures

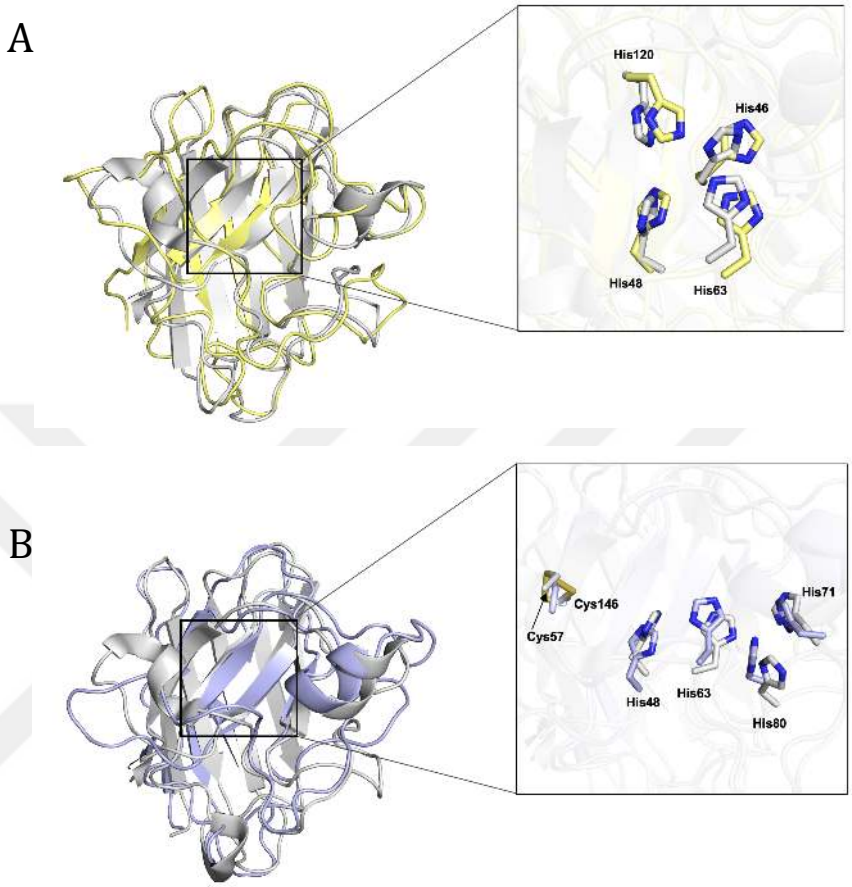

Figure 3.23 The comparison of active sites of SOD1^{WT}_ambient with apo structure (3ECU)
A) Superposition of chain A of both structures (Left panel), active site comparison of chain A (Top right panel), Pair-wise distance graph (Bottom right panel). B) The same representations for chain B.

To determine structural changes in each monomer of the obtained apo structure of SOD1^{WT} at ambient temperature, chain A and chain B of the structure were superimposed with two chains of apo (3ECU), zinc-bound (5YUL) and copper and zinc-bound (2C9V) (**Figure 3.23, 3.24 & 3.25**). For all three comparisons, His46, His48, His63 and His120 of chain A and Cys57, Cys146, His48, His63, His71 and His80 of chain B were used. Firstly, each monomer of our structure was compared with monomers of the apo structure of SOD1 (3ECU). The RMSD values for chains A and B were 1.29 Å and 1.35 Å. The superposition results showed significant difference in only His63 of chain A

(**Figure 3.23-A**). However, when we compare the active site residues in chain B, changes in the cysteine residues and His80 were seen (**Figure 3.23-B**).

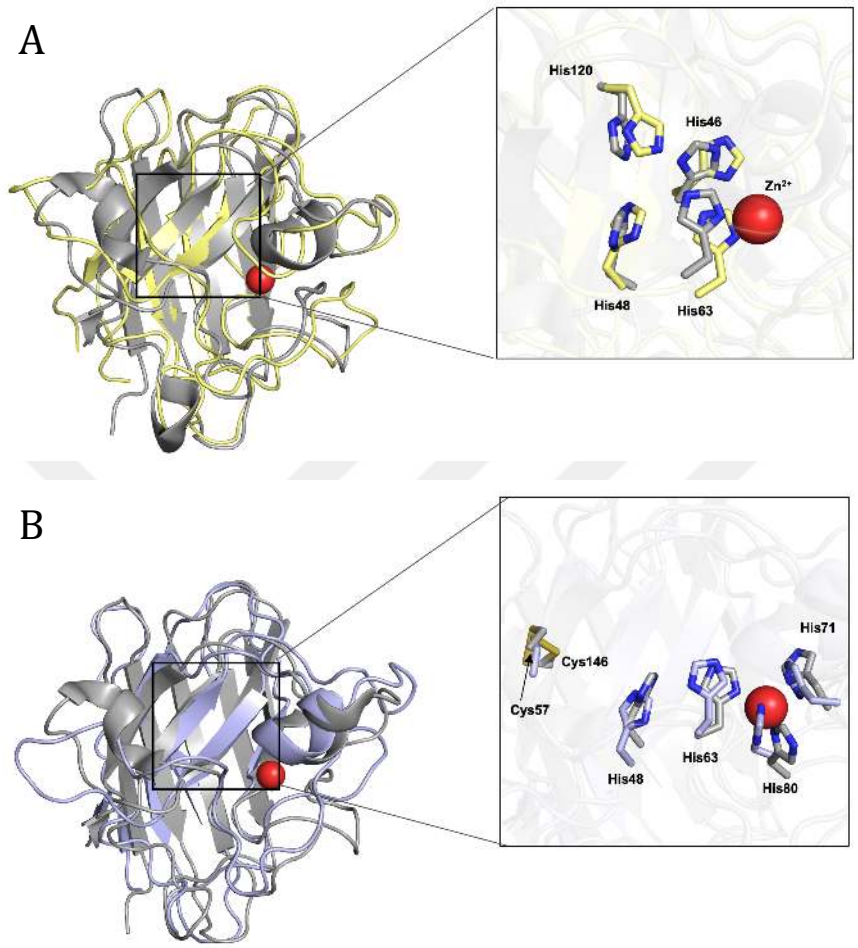

Figure 3.24 The comparison of active sites of SOD1^{WT}_ambient with zinc-bound structure (5YUL)
A) Superposition of chain A of both structures (Left panel), active site comparison of chain A (Top right panel), Pair-wise distance graph (Bottom right panel). B) The same representations for chain B.

The second previously reported structure compared with the new apo structure was zinc-bound SOD1 (5YUL). After alignment, the RMSD values of chains A and B were 1.25 and 1.17 Å. The superposition and active site comparison results of the new structure with 5YUL were similar to 3ECU, especially for chain A (**Figure 3.24**).

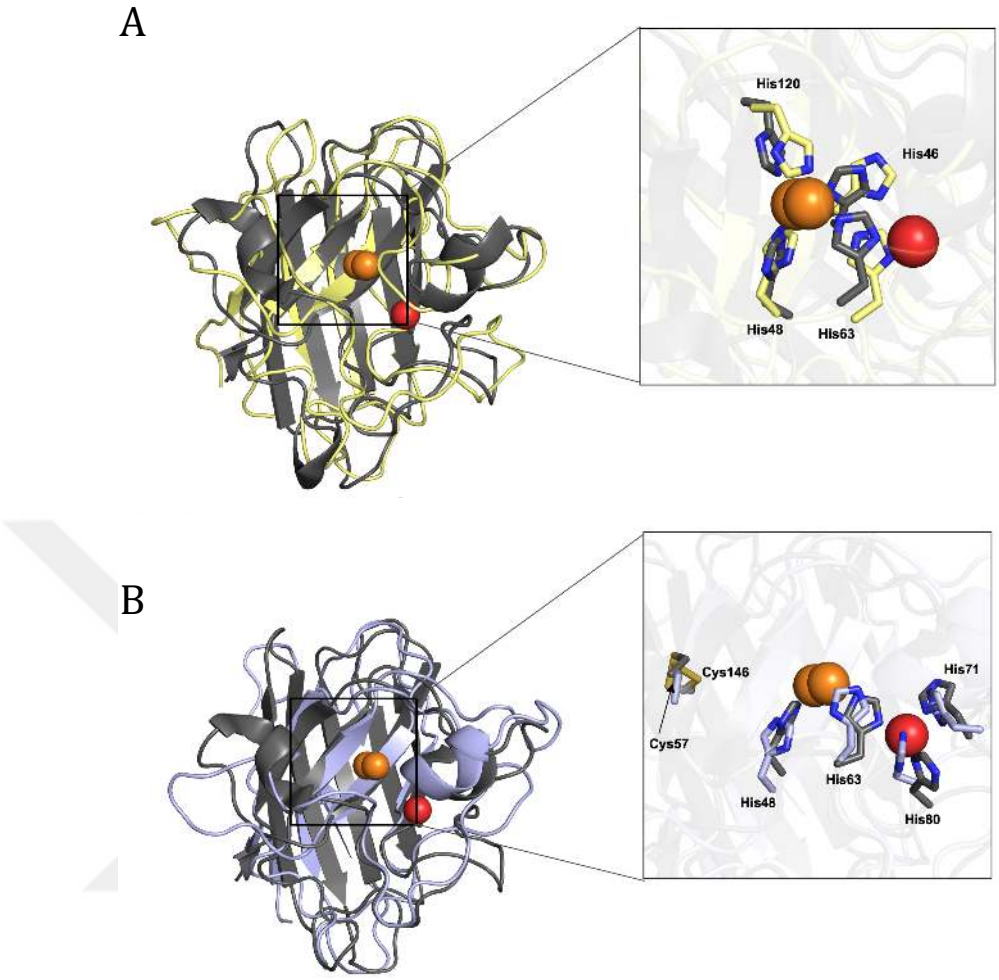

Figure 3.25 The comparison of active sites of SOD1^{WT}_ambient with copper and zinc-bound structure (2C9V)
A) Superposition of chain A of both structures (Left panel), active site comparison of chain A (Top right panel), Pair-wise distance graph (Bottom right panel). B) The same representations for chain B.

Finally, copper and zinc-bound structure was superposed with the new structure to show structural differences. The RMSD value for chain A was 1.24 Å which is the lowest for chain A compared to other structures (**Figure 3.25-A**). As a result of the alignment, the RMSD of chain B was 1.18 Å. In active site comparison, we could not see noticeable different results with the comparison of other structures' active site (**Figure 3.25-B**).

Table 3.3 X-ray crystallography statistics

Data Collection	
Beamline	Turkish Light Source (XRD)
Space Group	P 2_1 2_1 2_1
Cell Dimensions	
a, b, c (Å)	84.60, 123.07 , 153.23
α, β, γ (°)	90, 90, 90
CC1/2	0.21 (0.14)
CC*	0.59 (0.50)
R_{merge}	4.95 (5.73)
R_{meas}	5.46 (6.28)
Multiplicity /Redundancy	5.1 (5.5)
Completeness (%)	44.61 (50.18)
Refinement	
Resolution (A)	30.36 - 4.0 (4.143 - 4.0)
Reflections	6275 (689)
R_{work}	0.35 (0.35)
R_{free}	0.40 (0.39)
Number of atoms	
Protein	13332

Water	61
B-factors	
Protein	164.01
Water	79.34
R.m.s deviations (Å)	
Bonds	0.008
Angles	1.38
Ramachandran Plot	
Favored (%)	85.87
Allowed (%)	12.53
Outliers (%)	1.60

Chapter 4:
CONCLUSION AND DISCUSSION

In this study, we determined the first ambient temperature structure of apo $SOD1^{WT}$, a crucial antioxidant enzyme expressed in almost every cell at 4.00 Å resolution and in the P 21 21 21 space group (**Figure 3.12**). The structure was revealed in the dimeric form of SOD1. In the fully mature form of the protein, each monomer has eight stranded beta-barrel motifs, intra-subunit disulfide bond and Cu^{2+} and Zn^{2+} ions in its active site (Yang et al., 2018). The obtained structure was in apo form with a beta-barrel motif and an alpha-helix (**Figure 3.12 & Figure 3.13**). Structures of previously identified wild-type and mutant SOD1s at cryogenic temperatures were shown in their most stable states. However, SOD1 has a more flexible structure in the solution; it forms its fully active structure by undergoing a maturation process. The model for the maturation process for SOD1; (1) metal-free and disulfide bond-free monomer binds to Zn^{2+} to make it more stable, (2) binding Zn^{2+} ions recruit hCCS to bind Cu^{2+} and to form disulfide bond between Cys57 and Cys146 and (3) two monomers with metal ions and disulfide bond comes together with non-covalent hydrogen and hydrophobic interactions to make the most stable active form of the protein (Banci et al., 2012; Culik et al., 2018). This model suggests that intermediate protein forms might be seen in physiological conditions. The conformational changes between the two monomers in the resulting structure may indicate that wild-type SOD1 has a dynamic structure at room temperature.

The overall comparison of the dimer protein structure of our protein with apo, Zn^{2+}-bound and Cu^{2+}-Zn^{2+} bound SOD1 structures showed that RMSD values were unexpectedly high, even though the amino acid sequences of all structures were the same (**Figure 3.15**). Since all compared structures (3ECU, 5YUL and 2C9V) were at cryogenic temperature, they have a more stable structure than ours. Although these compared structures were supposed to be different forms of SOD1 (apo, Zn^{2+}, Cu^{2+}-Zn^{2+} bound structures), they were almost identical (**Figure 3.16**). It shows that X-ray crystallography methods at cryogenic temperatures allow seeing only the most stable conformation of the structure. In our experiment, we used the XtalCheck-S plate reader to collect data directly from crystals in the well at ambient temperature. We screened more than 100 crystals

from the replicate plates to get data to process. Two or three crystals from the well containing Wizard II #7 + 0.5 µl Additive screen #2 conditions. After collecting data, we merged data collected from different crystals with same space group and unit cell parameters. With this experiment, we determined a more flexible structure at ambient temperature compared to the other structures. When we compared chains of our structure to see differences at the monomeric level, RMSD values were lower than the dimeric structure alignment. The monomers of the new structure showed high similarity to the monomers of the previous structures, while the dimer structure was less similar to the other structures. In this situation, protein might be in the intermediate form before dimerization.

The active site residues of SOD1 provide a more stable structure for protein and helps to start the reaction. Six histidine residues (His46, His48, His63, His71, His80 and His120) are responsible for metal binding, two cysteine residues (Cys57 and 146) create a disulfide bond and two positively charged residues (Lys 136 and Arg143) located in the electrostatic loop coordinate to direct superoxide to the active site. Conformational changes were observed in all active site residues when we compared active sites of the chains of the new structures together and with other structures (**Figure 3.14 & Figure 3.23, 24 & 25**). Structural changes at side chains of histidine residues were rotational, with locations of histidine residues were almost the same in both chains of the protein. According to the results of active site comparison with previously identified structures, His63, which is a common residue for binding both Cu^{2+} and Zn^{2+} showed a more remarkable conformational change compared to other histidine residues. In both chains, the electron densities of Lys136 and Arg143 were not seem fully or partial. Since these residues are located electrostatic loop near to dimer interface and are thought to be necessary for stabilizing the structure and reaction of protein, missing electron density maps in these residues may suggest that the electrostatic loop might be flexible and change location during the dimerization process.

Non-covalent interactions between two chains of SOD1 create the dimeric structure of the protein. Especially four hydrogen bonds in the dimeric interface of SOD1 are essential for dimerization: between Ile151O (chain A) - Gly51N (chain B), Ile151N (chain A) – Gly114O (chain B), Gly51N (chain A) – Ile151O (chain B) and Gly114O (chain A) – Ile151N (chain B). We compared the hydrogen bond formation in the dimeric interface of the new structure with one of the most stable and high-quality structures of

SOD1 (PDB ID: 2C9V) to check the dimeric region of our new structure. The four hydrogen bonds were formed in the Cu^{2+} and Zn^{2+} bound structure (2C9V) within the range 2.7-2.9 A. In our structure, there was no hydrogen bond formation. The distances between Ile151O (chain A) - Gly51N (chain B), Ile151N (chain A) – Gly114O (chain B), Gly51N (chain A) – Ile151O (chain B) and Gly114O (chain A) – Ile151N (chain B) were 10.8 Å, 9.1 Å, 5.5 Å and 7.0 Å respectively (**Figure 3.17**). We also compared the dimeric interfaces of other five dimers of newly identified structure of SOD1 with 2C9V. All comparisons showed that the hydrogen bond formation was not observed in the dimeric interfaces of the six dimers of our structure (**Figure 3.18, 3.19, 3.20, 3.21 & 3.22)**. These results may suggest that the monomers of our structure are closed to each other, but the distances are not enough for the dimerization. In addition to the comparison of dimeric interface of the first dimer of our new structure, we showed there are different positions of the residues normally make hydrogen bonds in the dimeric region. Only two hydrogen bonds were observed after all these dimeric interface comparisons (**Figure 3.19 & 3.20**). These results may indicate that the different dimer formations can happen in SOD1 structure. These results also explained the unexpected high RMSD values of dimeric structure comparison between our structure and previous apo, Zn^{2+} and Cu^{2+}- Zn^{2+} bound structures.

All the results obtained from $SOD1^{WT}$ crystals showed that our structure was more flexible than other structures and did not complete the dimerization process. However, our study has some limitations; the diffraction data from the crystals was collected by a home source X-ray diffractometer and its completeness after refinement was 40%. In addition, in all the data we obtained, we saw that the diffraction could not go beyond 4 A. Dimerization can also be affected by His-tag at the N-terminus of SOD1. We also crystalized wild-type SOD1 without six histidine tags. Only weak diffraction was observed when we tried to collect data from crystals obtained from SOD1 w/o His-tag. In addition to $SOD1^{WT}$ crystals, we also crystalized $SOD1^{G93A}$ protein successfully. The same scenario happened to mutant form with the wild-type protein without His-tag. In future studies, the crystals obtained from these two proteins will be optimized with additional conditions and diffraction data will be collected at room temperature with the XtalCheck-S plate reader. In addition to all these, with this preliminary data obtained, as a future plan, data will be collected from more optimized crystals of both wild-type and

a mutant form of SOD1 obtained at room temperature with a more powerful X-ray source such as XFEL.

Misfolding of SOD1 does not only affect the function of this antioxidant protein in the cellular environment but also, it can cause aggregation and interactions of SOD1 with the proteins have different roles. One of the most critical interaction partners of SOD1 is VDAC1, a mitochondrial membrane protein. Misfolded SOD1 protein interacts with VDAC1 and decreases the conductance of this channel. The other interaction partner of SOD1, MIF, inhibits the misfolding and formation of amyloid-like fibrils. We planned to see these interactions of mutant SOD1 with VDAC1 and MIF by X-ray crystallography approaches. We successfully produced these proteins in *E. coli* BL21 Rosetta 2 strains within this aim. MIF was also purified with the Ni-NTA chromatography method and VDAC1 was refolded by the dropwise method (**Figure 3.5 & Figure 3.6**). After confirming the binding of these proteins with pull down assay, crystals will be obtained from the proteins in the future and X-ray diffraction data will be collected from these crystals at room temperature to show binding sites of SOD1 to these proteins. The information about binding sites will provide a perspective for further drug development studies targeting SOD1.

BIBLIOGRAPHY

Al-Chalabi A, Fang F, Hanby MF, Leigh PN, Shaw CE, Ye W, Rijsdijk F. 2010. An estimate of amyotrophic lateral sclerosis heritability using twin data. *Journal of Neurology, Neurosurgery & Psychiatry* **81**: 1324–1326.

Atsumi T. 1981. The ultrastructure of intramuscular nerves in amyotrophic lateral sclerosis. *Acta Neuropathologica* **55**: 193–198.

Banci L, Bertini I, Boca M, Girotto S, Martinelli M, Valentine JS, Vieru M. 2008. SOD1 and Amyotrophic Lateral Sclerosis: Mutations and Oligomerization. *PLoS ONE* **3**: e1677.

Banci L, Bertini I, Cantini F, Kozyreva T, Massagni C, Palumaa P, Rubino JT, Zovo K. 2012. Human superoxide dismutase 1 (hSOD1) maturation through interaction with human copper chaperone for SOD1 (hCCS). *Proceedings of the National Academy of Sciences* **109**: 13555–13560.

Bayrhuber M, Meins T, Habeck M, Becker S, Giller K, Villinger S, Vonrhein C, Griesinger C, Zweckstetter M, Zeth K. 2008. Structure of the human voltage-dependent anion channel. *Proceedings of the National Academy of Sciences* **105**: 15370–15375.

Bertolin C, Querin G, Bozzoni V, Martinelli I, de Bortoli M, Rampazzo A, Gellera C, Pegoraro E, Sorarù G. 2018. New *<scp>FIG</scp> 4* gene mutations causing aggressive <scp>ALS</scp>. *European Journal of Neurology* **25**.

Bloom BR, Bennett B. 1966. Mechanism of a Reaction in Vitro Associated with Delayed-Type Hypersensitivity. *Science (1979)* **153**: 80–82.

Brown RH, Al-Chalabi A. 2017. Amyotrophic Lateral Sclerosis. *New England Journal of Medicine* **377**: 162–172.

Bruijn LI, Houseweart MK, Kato S, Anderson KL, Anderson SD, Ohama E, Reaume AG, Scott RW, Cleveland DW. 1998. Aggregation and Motor Neuron Toxicity of an ALS-Linked SOD1 Mutant Independent from Wild-Type SOD1. *Science (1979)* **281**: 1851–1854.

Camara AKS, Zhou Y, Wen P-C, Tajkhorshid E, Kwok W-M. 2017. Mitochondrial VDAC1: A Key Gatekeeper as Potential Therapeutic Target. *Frontiers in Physiology* **8**.

Chatterjee M, Borst O, Walker B, Fotinos A, Vogel S, Seizer P, Mack A, Alampour-Rajabi S, Rath D, Geisler T, et al. 2014. Macrophage Migration Inhibitory Factor Limits

Activation-Induced Apoptosis of Platelets via CXCR7-Dependent Akt Signaling. *Circulation Research* **115**: 939–949.

Cherepkova OA, Lyutova EM, Gurvits BYa. 2006. Macrophage migration inhibitory factor: Isolation from bovine brain. *Biochemistry (Moscow)* **71**: 73–78.

Cheroni C, Marino M, Tortarolo M, Veglianese P, de Biasi S, Fontana E, Zuccarello LV, Maynard CJ, Dantuma NP, Bendotti C. 2009. Functional alterations of the ubiquitin-proteasome system in motor neurons of a mouse model of familial amyotrophic lateral sclerosis†. *Human Molecular Genetics* **18**: 82–96.

Chiò A, Logroscino G, Hardiman O, Swingler R, Mitchell D, Beghi E, Traynor BG, On Behalf of the Eurals Consortium. 2009. Prognostic factors in ALS: A critical review. *Amyotrophic Lateral Sclerosis* **10**: 310–323.

Cooper-Knock J, Hewitt C, Highley JR, Brockington A, Milano A, Man S, Martindale J, Hartley J, Walsh T, Gelsthorpe C, et al. 2012. Clinico-pathological features in amyotrophic lateral sclerosis with expansions in C9ORF72. *Brain* **135**: 751–764.

Cox LE, Ferraiuolo L, Goodall EF, Heath PR, Higginbottom A, Mortiboys H, Hollinger HC, Hartley JA, Brockington A, Burness CE, et al. 2010. Mutations in CHMP2B in Lower Motor Neuron Predominant Amyotrophic Lateral Sclerosis (ALS). *PLoS ONE* **5**: e9872.

Culik RM, Sekhar A, Nagesh J, Deol H, Rumfeldt JAO, Meiering EM, Kay LE. 2018. Effects of maturation on the conformational free-energy landscape of SOD1. *Proceedings of the National Academy of Sciences* **115**.

DeJesus-Hernandez M, Mackenzie IR, Boeve BF, Boxer AL, Baker M, Rutherford NJ, Nicholson AM, Finch NA, Flynn H, Adamson J, et al. 2011. Expanded GGGGCC Hexanucleotide Repeat in Noncoding Region of C9ORF72 Causes Chromosome 9p-Linked FTD and ALS. *Neuron* **72**: 245–256.

Deng H-X, Chen W, Hong S-T, Boycott KM, Gorrie GH, Siddique N, Yang Y, Fecto F, Shi Y, Zhai H, et al. 2011. Mutations in UBQLN2 cause dominant X-linked juvenile and adult-onset ALS and ALS/dementia. *Nature* **477**: 211–215.

Deng J, Yang M, Chen Y, Chen X, Liu J, Sun S, Cheng H, Li Y, Bigio EH, Mesulam M, et al. 2015. FUS Interacts with HSP60 to Promote Mitochondrial Damage. *PLOS Genetics* **11**: e1005357.

Donnelly CJ, Zhang P-W, Pham JT, Haeusler AR, Mistry NA, Vidensky S, Daley EL, Poth EM, Hoover B, Fines DM, et al. 2013. RNA Toxicity from the ALS/FTD C9ORF72 Expansion Is Mitigated by Antisense Intervention. *Neuron* **80**: 415–428.

Fecto F. 2011. <emph type="ital">SQSTM1</emph> Mutations in Familial and Sporadic Amyotrophic Lateral Sclerosis. *Archives of Neurology* **68**: 1440.

Furukawa Y, O'Halloran T v. 2005. Amyotrophic Lateral Sclerosis Mutations Have the Greatest Destabilizing Effect on the Apo- and Reduced Form of SOD1, Leading to Unfolding and Oxidative Aggregation. *Journal of Biological Chemistry* **280**: 17266–17274.

Gal J, Ström A-L, Kwinter DM, Kilty R, Zhang J, Shi P, Fu W, Wooten MW, Zhu H. 2009. Sequestosome 1/p62 links familial ALS mutant SOD1 to LC3 via an ubiquitin-independent mechanism. *Journal of Neurochemistry* **111**: 1062–1073.

Geula S, Ben-Hail D, Shoshan-Barmatz V. 2012. Structure-based analysis of VDAC1: N-terminus location, translocation, channel gating and association with anti-apoptotic proteins. *Biochemical Journal* **444**: 475–485.

Harry GJ, Kraft AD. 2008. Neuroinflammation and microglia: considerations and approaches for neurotoxicity assessment. *Expert Opinion on Drug Metabolism & Toxicology* **4**: 1265–1277.

Hickman S, Izzy S, Sen P, Morsett L, el Khoury J. 2018. Microglia in neurodegeneration. *Nature Neuroscience* **21**: 1359–1369.

Israelson A, Arbel N, da Cruz S, Ilieva H, Yamanaka K, Shoshan-Barmatz V, Cleveland DW. 2010. Misfolded Mutant SOD1 Directly Inhibits VDAC1 Conductance in a Mouse Model of Inherited ALS. *Neuron* **67**: 575–587.

Johnson JO, Mandrioli J, Benatar M, Abramzon Y, van Deerlin VM, Trojanowski JQ, Gibbs JR, Brunetti M, Gronka S, Wuu J, et al. 2010. Exome Sequencing Reveals VCP Mutations as a Cause of Familial ALS. *Neuron* **68**: 857–864.

Joyce PI, Fratta P, Fisher EMC, Acevedo-Arozena A. 2011. SOD1 and TDP-43 animal models of amyotrophic lateral sclerosis: recent advances in understanding disease toward the development of clinical treatments. *Mammalian Genome* **22**: 420–448.

Kawamata H, Magrané J, Kunst C, King MP, Manfredi G. 2008. Lysyl-tRNA Synthetase Is a Target for Mutant SOD1 Toxicity in Mitochondria. *Journal of Biological Chemistry* **283**: 28321–28328.

Kia A, McAvoy K, Krishnamurthy K, Trotti D, Pasinelli P. 2018. Astrocytes expressing ALS-linked mutant FUS induce motor neuron death through release of tumor necrosis factor-alpha. *Glia* **66**: 1016–1033.

Kodavati M, Wang H, Hegde ML. 2020. Altered Mitochondrial Dynamics in Motor Neuron Disease: An Emerging Perspective. *Cells* **9**: 1065.

Kuhle J, Lindberg RLP, Regeniter A, Mehling M, Steck AJ, Kappos L, Czaplinski A. 2009. Increased levels of inflammatory chemokines in amyotrophic lateral sclerosis. *European Journal of Neurology* **16**: 771–774.

Kwiatkowski TJ, Bosco DA, LeClerc AL, Tamrazian E, Vanderburg CR, Russ C, Davis A, Gilchrist J, Kasarskis EJ, Munsat T, et al. 2009. Mutations in the *FUS/TLS* Gene on Chromosome 16 Cause Familial Amyotrophic Lateral Sclerosis. *Science (1979)* **323**: 1205–1208.

Lagier-Tourenne C, Baughn M, Rigo F, Sun S, Liu P, Li H-R, Jiang J, Watt AT, Chun S, Katz M, et al. 2013. Targeted degradation of sense and antisense *C9orf72* RNA foci as therapy for ALS and frontotemporal degeneration. *Proceedings of the National Academy of Sciences* **110**.

Liu EY, Russ J, Wu K, Neal D, Suh E, McNally AG, Irwin DJ, van Deerlin VM, Lee EB. 2014. C9orf72 hypermethylation protects against repeat expansion-associated pathology in ALS/FTD. *Acta Neuropathologica* **128**: 525–541.

Majcher V, Goode A, James V, Layfield R. 2015. Autophagy receptor defects and ALS-FTLD. *Molecular and Cellular Neuroscience* **66**: 43–52.

Majounie E, Renton AE, Mok K, Dopper EG, Waite A, Rollinson S, Chiò A, Restagno G, Nicolaou N, Simon-Sanchez J, et al. 2012. Frequency of the C9orf72 hexanucleotide repeat expansion in patients with amyotrophic lateral sclerosis and frontotemporal dementia: a cross-sectional study. *The Lancet Neurology* **11**: 323–330.

Mattiazzi M, D'Aurelio M, Gajewski CD, Martushova K, Kiaei M, Beal MF, Manfredi G. 2002. Mutated Human SOD1 Causes Dysfunction of Oxidative Phosphorylation in Mitochondria of Transgenic Mice. *Journal of Biological Chemistry* **277**: 29626–29633.

Merk M, Zierow S, Leng L, Das R, Du X, Schulte W, Fan J, Lue H, Chen Y, Xiong H, et al. 2011. The *D* -dopachrome tautomerase (*DDT*) gene product is a cytokine and functional homolog of macrophage migration inhibitory factor (MIF). *Proceedings of the National Academy of Sciences* **108**.

Mulder D, Kurland L, Offord K, Beard C. 1986. Familial adult motor neuron disease: amyotrophic lateral sclerosis. *Neurology* **36**: 511–517.

Murakami T, Nagano I, Hayashi T, Manabe Y, Shoji M, Setoguchi Y, Abe K. 2001. Impaired retrograde axonal transport of adenovirus-mediated E. coli LacZ gene in the mice carrying mutant SOD1 gene. *Neuroscience Letters* **308**: 149–152.

Nassif M, Woehlbier U, Manque PA. 2017. The Enigmatic Role of C9ORF72 in Autophagy. *Frontiers in Neuroscience* **11**.

Nishitoh H, Kadowaki H, Nagai A, Maruyama T, Yokota T, Fukutomi H, Noguchi T, Matsuzawa A, Takeda K, Ichijo H. 2008. ALS-linked mutant SOD1 induces ER stress- and ASK1-dependent motor neuron death by targeting Derlin-1. *Genes & Development* **22**: 1451–1464.

Palomo GM, Granatiero V, Kawamata H, Konrad C, Kim M, Arreguin AJ, Zhao D, Milner TA, Manfredi G. 2018. Parkin is a disease modifier in the mutant <scp>SOD</scp> 1 mouse model of <scp>ALS</scp>. *EMBO Molecular Medicine* **10**.

Pasinelli P, Belford ME, Lennon N, Bacskai BJ, Hyman BT, Trotti D, Brown RH. 2004a. Amyotrophic Lateral Sclerosis-Associated SOD1 Mutant Proteins Bind and Aggregate with Bcl-2 in Spinal Cord Mitochondria. *Neuron* **43**: 19–30.

Pasinelli P, Belford ME, Lennon N, Bacskai BJ, Hyman BT, Trotti D, Brown RH. 2004b. Amyotrophic Lateral Sclerosis-Associated SOD1 Mutant Proteins Bind and Aggregate with Bcl-2 in Spinal Cord Mitochondria. *Neuron* **43**: 19–30.

Pasupuleti V, Du W, Gupta Y, Yeh I-J, Montano M, Magi-Galuzzi C, Welford SM. 2014. Dysregulated D-dopachrome Tautomerase, a Hypoxia-inducible Factor-dependent Gene, Cooperates with Macrophage Migration Inhibitory Factor in Renal Tumorigenesis. *Journal of Biological Chemistry* **289**: 3713–3723.

Perlson E, Maday S, Fu M, Moughamian AJ, Holzbaur ELF. 2010. Retrograde axonal transport: pathways to cell death? *Trends in Neurosciences* **33**: 335–344.

Pickles S, Destroismaisons L, Peyrard SL, Cadot S, Rouleau GA, Brown RH, Julien J-P, Arbour N, vande Velde C. 2013. Mitochondrial damage revealed by immunoselection for ALS-linked misfolded SOD1. *Human Molecular Genetics* **22**: 3947–3959.

Prasad A, Bharathi V, Sivalingam V, Girdhar A, Patel BK. 2019. Molecular Mechanisms of TDP-43 Misfolding and Pathology in Amyotrophic Lateral Sclerosis. *Frontiers in Molecular Neuroscience* **12**.

Renton AE, Chiò A, Traynor BJ. 2014. State of play in amyotrophic lateral sclerosis genetics. *Nature Neuroscience* **17**: 17–23.

Renton AE, Majounie E, Waite A, Simón-Sánchez J, Rollinson S, Gibbs JR, Schymick JC, Laaksovirta H, van Swieten JC, Myllykangas L, et al. 2011. A Hexanucleotide Repeat Expansion in C9ORF72 Is the Cause of Chromosome 9p21-Linked ALS-FTD. *Neuron* **72**: 257–268.

Rosen DR, Siddique T, Patterson D, Figlewicz DA, Sapp P, Hentati A, Donaldson D, Goto J, O'Regan JP, Deng H-X, et al. 1993. Mutations in Cu/Zn superoxide dismutase gene are associated with familial amyotrophic lateral sclerosis. *Nature* **362**: 59–62.

Rostovtseva T, Colombini M. 1996. ATP Flux Is Controlled by a Voltage-gated Channel from the Mitochondrial Outer Membrane. *Journal of Biological Chemistry* **271**: 28006–28008.

Rostovtseva T, Colombini M. 1997. VDAC channels mediate and gate the flow of ATP: implications for the regulation of mitochondrial function. *Biophysical Journal* **72**: 1954–1962.

Rostovtseva TK, Sheldon KL, Hassanzadeh E, Monge C, Saks V, Bezrukov SM, Sackett DL. 2008. Tubulin binding blocks mitochondrial voltage-dependent anion channel and regulates respiration. *Proceedings of the National Academy of Sciences* **105**: 18746–18751.

Sanhueza M, Zechini L, Gillespie T, Pennetta G. 2014. Gain-of-function mutations in the ALS8 causative gene VAPB have detrimental effects on neurons and muscles. *Biology Open* **3**: 59–71.

Sea K, Sohn SH, Durazo A, Sheng Y, Shaw BF, Cao X, Taylor AB, Whitson LJ, Holloway SP, Hart PJ, et al. 2015. Insights into the Role of the Unusual Disulfide Bond in Copper-Zinc Superoxide Dismutase. *Journal of Biological Chemistry* **290**: 2405–2418.

Shimizu S, Matsuoka Y, Shinohara Y, Yoneda Y, Tsujimoto Y. 2001. Essential Role of Voltage-Dependent Anion Channel in Various Forms of Apoptosis in Mammalian Cells. *Journal of Cell Biology* **152**: 237–250.

Shteinfer-Kuzmine A, Argueti S, Gupta R, Shvil N, Abu-Hamad S, Gropper Y, Hoeber J, Magrì A, Messina A, Kozlova EN, et al. 2019. A VDAC1-Derived N-Terminal Peptide Inhibits Mutant SOD1-VDAC1 Interactions and Toxicity in the SOD1 Model of ALS. *Frontiers in Cellular Neuroscience* **13**.

Shvil N, Banerjee V, Zoltsman G, Shani T, Kahn J, Abu-Hamad S, Papo N, Engel S, Bernhagen J, Israelson A. 2018. MIF inhibits the formation and toxicity of misfolded SOD1 amyloid aggregates: implications for familial ALS. *Cell Death & Disease* **9**: 107.

Smith BN, Vance C, Scotter EL, Troakes C, Wong CH, Topp S, Maekawa S, King A, Mitchell JC, Lund K, et al. 2015. Novel mutations support a role for Profilin 1 in the pathogenesis of ALS. *Neurobiology of Aging* **36**: 1602.e17-1602.e27.

Song S, Xiao Z, Dekker FJ, Poelarends GJ, Melgert BN. 2022. Macrophage migration inhibitory factor family proteins are multitasking cytokines in tissue injury. *Cellular and Molecular Life Sciences* **79**: 105.

Stifani N. 2014. Motor neurons and the generation of spinal motor neuron diversity. *Frontiers in Cellular Neuroscience* **8**.

Strong MJ, Volkening K, Hammond R, Yang W, Strong W, Leystra-Lantz C, Shoesmith C. 2007. TDP43 is a human low molecular weight neurofilament (hNFL) mRNA-binding protein. *Molecular and Cellular Neuroscience* **35**: 320–327.

Talbot K, Feneberg E, Scaber J, Thompson AG, Turner MR. 2018. Amyotrophic lateral sclerosis: the complex path to precision medicine. *Journal of Neurology* **265**: 2454–2462.

Talbott EO, Malek AM, Lacomis D. 2016. The epidemiology of amyotrophic lateral sclerosis. pp. 225–238.

Taylor JP, Brown RH, Cleveland DW. 2016. Decoding ALS: from genes to mechanism. *Nature* **539**: 197–206.

Tiwari A, Xu Z, Hayward LJ. 2005. Aberrantly Increased Hydrophobicity Shared by Mutants of Cu,Zn-Superoxide Dismutase in Familial Amyotrophic Lateral Sclerosis. *Journal of Biological Chemistry* **280**: 29771–29779.

Tong J, Huang C, Bi F, Wu Q, Huang B, Liu X, Li F, Zhou H, Xia X-G. 2013. Expression of ALS-linked TDP-43 mutant in astrocytes causes non-cell-autonomous motor neuron death in rats. *The EMBO Journal* **32**: 1917–1926.

Tsujimoto Y, Shimizu S. 2000. VDAC regulation by the Bcl-2 family of proteins. *Cell Death & Differentiation* **7**: 1174–1181.

Vahsen BF, Gray E, Thompson AG, Ansorge O, Anthony DC, Cowley SA, Talbot K, Turner MR. 2021. Non-neuronal cells in amyotrophic lateral sclerosis — from pathogenesis to biomarkers. *Nature Reviews Neurology* **17**: 333–348.

vande Velde C, Miller TM, Cashman NR, Cleveland DW. 2008. Selective association of misfolded ALS-linked mutant SOD1 with the cytoplasmic face of mitochondria. *Proceedings of the National Academy of Sciences* **105**: 4022–4027.

Wang J, Xu G, Borchelt DR. 2002. High Molecular Weight Complexes of Mutant Superoxide Dismutase 1: Age-Dependent and Tissue-Specific Accumulation. *Neurobiology of Disease* **9**: 139–148.

Wang W, Li L, Lin W-L, Dickson DW, Petrucelli L, Zhang T, Wang X. 2013. The ALS disease-associated mutant TDP-43 impairs mitochondrial dynamics and function in motor neurons. *Human Molecular Genetics* **22**: 4706–4719.

Wang W, Wang L, Lu J, Siedlak SL, Fujioka H, Liang J, Jiang S, Ma X, Jiang Z, da Rocha EL, et al. 2016. The inhibition of TDP-43 mitochondrial localization blocks its neuronal toxicity. *Nature Medicine* **22**: 869–878.

Wang Y, Xu E, Musich PR, Lin F. 2019. Mitochondrial dysfunction in neurodegenerative diseases and the potential countermeasure. *CNS Neuroscience & Therapeutics* **25**: 816–824.

Watanabe M, Dykes-Hoberg M, Cizewski Culotta V, Price DL, Wong PC, Rothstein JD. 2001. Histological Evidence of Protein Aggregation in Mutant SOD1 Transgenic Mice and in Amyotrophic Lateral Sclerosis Neural Tissues. *Neurobiology of Disease* **8**: 933–941.

Yang F, Wang H, Logan DT, Mu X, Danielsson J, Oliveberg M. 2018. The Cost of Long Catalytic Loops in Folding and Stability of the ALS-Associated Protein SOD1. *J Am Chem Soc* **140**: 16570–16579.

Yang Y, Hentati A, Deng H-X, Dabbagh O, Sasaki T, Hirano M, Hung W-Y, Ouahchi K, Yan J, Azim AC, et al. 2001. The gene encoding alsin, a protein with three guanine-nucleotide exchange factor domains, is mutated in a form of recessive amyotrophic lateral sclerosis. *Nature Genetics* **29**: 160–165.

Ying H, Yue BYJT. 2016. Optineurin: The autophagy connection. *Experimental Eye Research* **144**: 73–80.

Appendix A: CHEMICALS

Chemicals and Media Components	Supplier Company
Acetic Acid	ISOLAB
Acrylamide/Bis-acrylamide	Bio-Rad
APS	Sigma-Aldrich
BME	Merck
Chloramphenicol	GOLDBIO
Coomassie Brilliant Blue	Bio-Rad
DTT	Roche
Ethanol	ISOLAB
Glycerol	ISOLAB
Glycine	ISOLAB
Imidazole	Biofroxx
IPTG	GOLDBIO
Kanamycin	GOLDBIO
LB	Thermo Fisher
Lysozyme	Sigma-Aldrich
LB Agar	Caisson
NaCl	ISOLAB
NaOH	ISOLAB
HCl	ISOLAB
Ni-NTA Resin	QIAGEN
Paraffin Oil	TEKKİM
PMSF	GOLDBIO
SDS	ISOLAB
TEMED	Sigma-Aldrich
Thrombin Protease	Sigma-Aldrich
Tris-HCl	Sigma-Aldrich
Triton X-100	Sigma-Aldrich
Tryptone	BD Biosciences
Yeast Extract	BD Biosciences

Appendix B: EQUIPMENT

Equipment	**Supplier Company**
AKTA GO	Cytiva
Amicon® Ultra-15 Centrifugal Filter Unit	Merck Millipore
Beckman Allegra 15R Centrifuge	Beckman Coulter
Beckman Avanti J-26S	Beckman Coulter
Beckman OptimaTM L-80 XP Ultracentrifuge	Beckman Coulter
Beckman Ti45 Rotor	Beckman Coulter
Branson W250 Sonifier	Branson
Cellulose Dialysis Tubing	Thermo Scientific
Cryovials	Wuxi NEST Biotechnology
Innova 44R	Eppendorf New Brunswick
Innova 4430R	Eppendorf New Brunswick
Kimwipes	Kimberly-Clark
Nanodrop2000c	Thermo Scientific
Superdex 200 Increase 10/300 GL	Cytiva
Terasaki Plate	Greiner Bio
TGX-Mini Protean Gradient SDS-PAGE System	Bio-Rad
Ultra-Pure Water System	Merck Millipore